Gravity wave induced cross-isentropic mixing: A DEEPWAVE case study

Hans-Christoph Lachnitt[1], Peter Hoor[1], Daniel Kunkel[1], Martina Bramberger[2], Andreas Dörnbrack[3], Stefan Müller[1,4], Philipp Reutter[1], Andreas Giez[3], Thorsten Kaluza[1], and Markus Rapp[3]

[1]Institute for Atmospheric Physics, Johannes Gutenberg University Mainz, Germany
[2]NorthWest Research Associates, Boulder, USA
[3]Institute of Atmospheric Physics, German Aerospace Center (DLR) Oberpfaffenhofen, Germany
[4]now at enviscope GmbH, Frankfurt/Main, Germany

Correspondence: Lachnitt, Hans-Christoph (hlachnit@uni-mainz.de)

Abstract. Orographic gravity waves (i.e. mountain waves) can potentially lead to cross-isentropic fluxes of trace gases via the generation of turbulence. During the DEEPWAVE (Deep Propagating Gravity Wave Experiment) campaign in July 2014 we performed tracer measurements of carbon monoxide (CO) and nitrous oxide (N_2O) above the Southern Alps during periods of gravity wave activity. The measurements were taken along two stacked levels at 7.9 km in the troposphere and 10.9 km in the stratosphere. A detailed analysis of the observed wind components shows ~~,~~ that both flight legs were affected by vertically propagating gravity waves with momentum deposition and energy dissipation between the two legs. Corresponding tracer measurements indicate turbulent mixing in the region of gravity wave occurrence.

For the stratospheric data we identified mixing leading to a change of the cross-isentropic tracer gradient of N_2O from the upstream to the downstream region of the Southern Alps. Based on the quasi-inert tracer N_2O we identified two distinct layers in the stratosphere with different chemical composition on different isentropes as given by constant potential temperature Θ. The CO-N_2O relationship clearly indicates that irreversible mixing between these two layers occurred. Further we found a significant change of the vertical profiles of N_2O ~~-~~with respect to Θ ~~-profiles~~ from the upstream to the downstream side above the Southern Alps ~~with different gradients of the -Θ-relation~~ just above the tropopause. A scale-dependent gradient analysis reveals that this ~~gradient change~~ cross-isentropic gradient change of N_2O is triggered in the region of gravity wave occurrence. The power spectra of the in-situ measured vertical wind, Θ, and N_2O indicate the occurrence of turbulence above the mountains associated with the gravity waves in the stratosphere. The estimated eddy dissipation rate based on the measured three dimensional wind indicates a weak intensity of turbulence in the stratosphere above the mountain ridge. ~~The -~~The Θ-N_2O-relation downwind the Alps modified by the gravity wave activity provides clear evidence that trace gas fluxes, which were deduced from wavelet co-spectra of vertical wind and N_2O are at least in part cross-isentropic.

Our findings thus indicate that orographic waves led to turbulent mixing on both flight legs in the troposphere and in the stratosphere. Despite only weak turbulence during the stratospheric leg, the ~~cross isentropic~~ cross-isentropic gradient and the related composition change on isentropic surfaces from upstream to downstream the mountain unambiguously conserves the effect of turbulent mixing by gravity wave activity ~~before~~ on the trace gas distribution prior the measurements. This finally

leads to irreversible ~~diabatic~~ (i.e. diabatic) trace gas fluxes across isentropes and thus has a persistent effect on the ~~UTLS~~ upper troposphere / lower stratosphere (UTLS) trace gas composition.

1 Introduction

Orographic gravity waves play an important role for the thermal and dynamical structure of the atmosphere and ~~may~~ affect the large scale stratospheric circulation ~~(e.g. Smith et al., 2008; Fritts and Alexander, 2003; Kim et al., 2003; Rapp et al., 2021)~~ (e.g. Smith et al., 2008; Fritts and Alexander, 2003; Kim et al., 2003; Alexander and Grimsdell, 2013; Rapp et al., 2021). Many observations of stratospheric gravity waves are based on satellite observations (e.g. Alexander et al., 2008; Geller et al., 2013; Ern et al., 2018). However, in the ~~upper troposphere/lower stratosphere (UTLS)~~ UTLS observations of gravity waves from aircraft and balloon soundings are essential for process studies beyond the resolution of satellites (e.g. Podglajen et al., 2016; Krisch et al., 2017; Wright and Banyard, 2020; Rapp et al., 2021). ~~They~~ Gravity waves propagate across the UTLS where static stability increases at the tropopause (Woods and Smith, 2010). Gravity waves may locally lead to the generation of convective instabilities (Lane and Sharman, 2006) or dynamical instability induced by vertical shear of the horizontal wind (Panofsky et al., 1968; Kunkel et al., 2014; Söder et al., 2021). Both types of instabilities may lead to the occurrence of turbulence, particularly when wave breaking occurs with potential subsequent mixing of trace species (Pavelin et al., 2002; Whiteway et al., 2003).

The tropopause as a central feature of the UTLS acts as a dynamical barrier for transport of species and the formation of trace gas gradients at the tropopause (e.g. Gettelman et al., 2011; Woiwode et al., 2018; Hoor et al., 2002; Pan et al., 2004). To overcome this dynamical barrier diabatic processes are required, which can be associated with radiation driven processes or phase transitions of water. ~~In addition~~ Wave breaking may cause diabatic transport and scale breakdown in the tracer structure with subsequent mixing of tracers by molecular diffusion (e.g. Balluch and Haynes, 1997).

In addition, turbulence occurrence, associated with wind shear above the tropopause ~~(Shapiro, 1980; Söder et al., 2021; Kaluza et al., 2021; Lilly et al., 1974) provides an efficient process for~~ (Shapiro, 1980; Söder et al., 2021; Kaluza et al., 2021, 2022; Lilly et al., 1974) provides such another efficient diabatic process. It leads to cross-isentropic mixing and thus irreversible trace gas exchange at the tropopause. We will use the term 'cross-isentropic' to emphasize the irreversible (entropy changing and therefore diabatic) nature of this process. Further the term 'cross-isentropic' allows to distinguish from 'quasi-isentropic mixing'. The latter is driven by synoptic and planetary waves leading to stirring and mixing best approximated along isentropes.

Diabatic processes lead to an irreversible redistribution of tracers which must be therefore cross-isentropic providing a tracer flux crossing isentropes. Turbulence at the tropopause can be generated by a number of processes, e.g. strong shear at the jet streams (e.g. Kaluza et al., 2021), convection (Wang, 2003; Mullendore et al., 2005; Homeyer et al., 2017) or frontal uplift leading to strong vertical convergence of the horizontal wind (Panofsky et al., 1968; Söder et al., 2021) and the generation of gravity waves (e.g., Whiteway et al., 2003; Wang, 2003).

The effect of orographic waves on tracer transport and mixing and the emerging tracer redistributions has been frequently discussed (Schilling et al., 1999; Heller et al., 2017; Moustaoui et al., 2010; Zhang et al., 2015; Podglajen et al., 2017; Grubišić et al., 2008; Woiwode et al., 2018). Observational studies mainly addressed the analysis of local kinematic fluxes using the covariance of the local vertical winds and the tracer fields (Shapiro, 1980; Schilling et al., 1999). Based on airborne observations in a tropopause fold, Shapiro (1980) identified ozone and particle fluxes in regions of turbulence ~~occurrence~~ and shear. They estimated vertical turbulent tracer fluxes by approximating the change of the mean tracer flux by the divergence of the ~~turbulent vertical~~ vertical turbulent tracer flux. This approach has been used to derive mountain wave induced tracer fluxes using the flux divergence approach between two flight legs (with altitude differences of typically 1000 m) providing evidence for a vertical flux of carbon monoxide (Schilling et al., 1999) or water ~~vapour~~ vapor (Heller et al., 2017).

Direct observations of gravity wave induced ~~vertical~~ cross-isentropic tracer ~~transport~~ mixing are sparse, since this requires high resolution measurements of passive tracers (i.e. tracers without chemical or microphysical sources or sinks) exactly in the region of turbulence occurrence associated with these waves. Kinematic fluxes based on the covariance of the local vertical wind and the passive tracers are not necessarily irreversible. Analysis of the relation between tracer mixing and orographic wave activity (Moustaoui et al., 2010; Mahalov et al., 2011) highlighted the importance of the local tropopause structure for the interpretation of fluxes. Moustaoui et al. (2010) concluded on the basis of in-situ observations that the layers within the UTLS including the tropopause may behave like material surfaces and that vertical displacements are largely reversible despite the occurrence of gravity waves. They further pointed out that the observed tracer characteristics are the result of a non-linear interaction between synoptic-scale waves modulated by shorter gravity waves, leading first to reversible transport and tracer mixing.

~~This study steps in here to provide~~ This study provides evidence on the basis of observed passive tracers that the breaking of mountain waves can lead to diabatic tracer redistribution in the tropopause region by cross-isentropic mixing. We ~~will~~ investigate how orographic gravity wave induced turbulence leads to a ~~non-local~~ persistent effect on the UTLS composition downwind of the turbulent mixing region.

The paper is ~~organised~~ organized as follows: First we will describe the measurements and techniques, and will briefly introduce the DEEPWAVE project and the meteorological conditions during the flight. Section 3 will focus on the observations and the identification of mixing from tracer measurements of N_2O and CO. In section 4 we will identify the effect of cross-isentropic mixing and use different methods to show that gravity wave induced turbulence and subsequent mixing has affected the observed tracer-Θ relationship with a persistent impact on the composition in the downstream side of the mountain ridge. The results will be analyzed for ~~non-isentropic~~ cross-isentropic transport followed by a discussion.

2 Data and Methods

2.1 Campaign and instrumentation

The measurements were performed in the frame of the DEEPWAVE (Deep Propagating Gravity Wave Experiment) mission in summer 2014 over New Zealand (Fritts et al., 2016; Gisinger et al., 2017). The project combined a comprehensive set of ground-based measurements as well as airborne measurements by the NSF (National Science Foundation) / NCAR (National Center for Atmospheric Research) Gulfstream GV HIAPER (High-performance Instrumented Airborne Platform for Environmental Research) and German DLR (Deutsches Zentrum für Luft- und Raumfahrt) Dassault Falcon 20E aircraft. Airborne measurements were carried out from Christchurch during June and July 2014 ~~and covered the upper troposphere and the lower stratosphere providing~~ that covered the UTLS and provided remote sensing data up to 80 km. The majority of the measurements focused on the Southern Alps to study the evolution of mountain waves from their source to the breaking regions in the mesosphere. The two aircraft partly performed coordinated flights in the tropopause region to study the propagation and potential dissipation of gravity waves in this region. During the 12. July, which is the day of the analysis in this paper no HIAPER flight was performed.

2.2 Aircraft Measurements

Tracer measurements of N_2O and CO were performed using the ‘University MAinz Quantum Cascade Absorption Spectrometer (UMAQS, Müller et al., 2015) onboard the DLR Falcon. The instrument consists of a Harriott cell with a path length of 36 m. We detected N_2O and CO at wavenumbers of 2002.75 cm^{-1} and 2003.16 cm^{-1}, respectively, by scanning with a frequency of 9 kHz across the absorption lines at a cell pressure of 50 hPa. ~~The instrument~~ UMAQS is capable of simultaneously measuring the species N_2O and CO reported here as volume mixing ratios in ppbv with a temporal resolution of 10 Hz ultimately limited by the flow speed and purging time of the cell. ~~The instrument is~~ We apply in-situ ~~calibrated~~ calibrations using secondary standards of compressed ambient air which are traced to primary standards of NOAA (National Oceanic and Atmospheric Administration) prior and after the campaign. The precision of the data (given here for the 1 Hz averaged data) is on the order of 0.05 ppbv (~~1~~ 1 standard deviation σ) for N_2O and CO, respectively.

We further use measurements of the basic atmospheric state parameters at 10 Hz provided by the Falcon aircraft (Krautstrunk and Giez, 2012). The three-dimensional wind is deduced from a 5-hole gust probe located in the noseboom providing true air speed and the ground speed from the inertial system (Mallaun et al., 2015). For the vertical wind component an uncertainty of ± 0.3 m s^{-1} is estimated. The true static air temperature is provided with a measurement uncertainty of ± 0.5 K.

2.3 Meteorological analysis data

To support our analysis and obtain information of the synoptic background we used ECMWF (European Center for Medium-Range Weather Forecast) IFS (Integrated Forecasting System) operational analysis data. The data are available every six hours and have been interpolated on a horizontal grid with a spacing of 0.125° for our analysis. In total the model has 137 vertical hybrid sigma-pressure levels from the surface up to 0.01 hPa. The vertical grid spacing is about 300 m in the tropopause region. For our analysis the model data are linearly interpolated in time and space onto the location of the flight track.

2.4 Wavelet analyses

The wavelet analysis is a tool for the spectral analysis of time series data (Torrence and Compo, 1998). The advantage over Fourier analysis is the ability to show information in time and frequency space. Wavelet analysis has frequently been used for the analysis of gravity waves (e.g., Bramberger et al., 2017; Zhang et al., 2015; Woods and Smith, 2011, 2010). The wavelet basis function which we use in this study is the Morlet wavelet with non-dimensional frequency $\omega_0 = 6$ as defined in Torrence and Compo (1998). To reveal periods with significant wavelet power we determined the 95% confidence level (which is equivalent to the 5% significant level) in the respective analyses below as described in Torrence and Compo (1998). The wavelet cospectrum can be used to ~~analyse~~ analyze spectral characteristics of turbulent fluxes (e.g. Mauder et al., 2007; Zhang et al., 2015). The wavelet cospectrum W^{AB} of two time series A and B with the wavelet transforms W^A and W^B is defined as the real part of the cross wavelet transformation

$$W_n^{AB}(s) = \Re\left\{W_n^A(s) W_n^{B*}(s)\right\} \tag{1}$$

where the asterisk denotes the complex conjugation, n a local time index and s the wavelet scale (Torrence and Compo, 1998; Liu et al., 2007).

Another tool which we use in this study is the wavelet coherence R^2. It represents the covariance between the two time series A and B and can be used to identify frequency and time intervals with strong and weak coherence between the variations of the two data sets. The wavelet coherence is defined as

$$R_n^2(s) = \frac{\left|S\left(s^{-1} W_n^{AB}(s)\right)\right|^2}{S\left(s^{-1}\left|W_n^A(s)\right|^2\right) \cdot S\left(s^{-1}\left|W_n^B(s)\right|^2\right)} \tag{2}$$

where S is a smoothing operator in space and time (for further details, see e.g., Torrence and Compo, 1998; Grinsted et al., 2004; Jevrejeva et al., 2003).

3 Observations and meteorological situation during FF09

3.1 Meteorological situation on 12. July 2014

~~Geopotential height (color) and potential temperature (dashed) at the 250 hPa surface with the flight track for research flight FF09 during 12. July 2014, 18:00 UTC. The red arrows indicate the flight direction.~~ In this study we focus on research flight FF09 of the Falcon aircraft on the 12. July 2014 starting at 17:15 UTC to 20:15 UTC (Fig. ~~??~~1). The goal of this flight was to investigate the dynamical and chemical structure of the atmosphere in the vicinity of tropopause during a mountain wave event (Gisinger et al., 2017; Smith et al., 2016). As can be seen in Fig. ~~??~~ 1 a rectangular pattern was flown clockwise to measure different wave responses in the northern and middle part of the Southern Island of New Zealand at two different pressure levels

(330 hPa and 260 hPa, Fig. 1) corresponding to approximately 7.9 km and 10.9 km pressure altitude. The time between two vertically stacked legs at the same location was 75 minutes (Fig. 2).

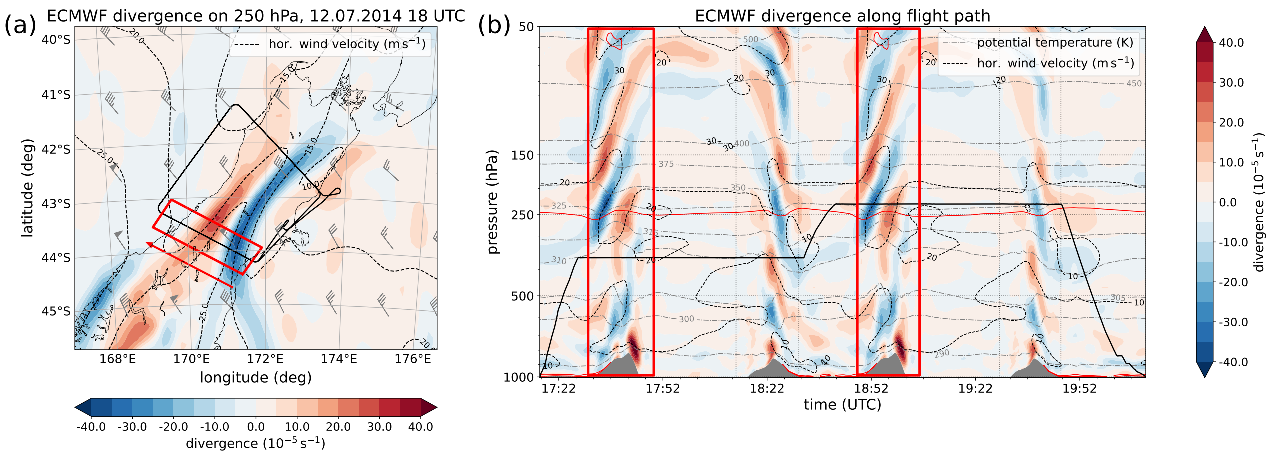

Figure 1. Divergence of the ECMWF horizontal wind during the time of flight (a) at 250 hPa and (b) as vertical cross section along the flight track indicating the signature of gravity waves over the Southern Alps. The solid red line denotes the -2 pvu isoline, the black dashed lines ~~denotes~~ denote contours of the horizontal wind velocity (10, 15, 20, 25 m s^{-1} in (a) and 10, 20, 30 m s^{-1} in (b)) and the gray dashed lines in (b) ~~denotes~~ denote contours of potential temperature. Regions of interest are marked by red rectangles and the red arrow in (a) indicates the clockwise flight direction.

According to Gisinger et al. (2017) the synoptic situation can be characterized by a trough located west of New Zealand with a weak surface low south of the Islands causing northwesterly winds in the troposphere (TNW regime, ~~their Fig.~~ Figure 2e in Gisinger et al. (2017)). In the upper level at 250 hPa at the eastern side of the approaching upper level trough a weak gradient of the geopotential height led to a northwesterly flow with moderate horizontal winds of typically 20 m s^{-1} along the southern flight legs (with 30 m s^{-1} above the mountain ridge). The tropopause became relatively flat in the region and at the time of the measurements (Fig. 1~~b).~~ (b)). These conditions led to the excitation of mountain waves and generated varying and moderate gravity wave responses over the South Island (Gisinger et al., 2017). Figure 1~~a~~ (a) shows the divergence of the ECMWF horizontal wind at 250 hPa at 18:00 UTC which corresponds roughly to the time of flight. The vertical cross section interpolated in time and space along the flight path shows a wave pattern above the mountain ridge indicating the excitation and propagation of orographic gravity waves, which propagate deep into the stratosphere (Fig. 1~~b~~(b)).

It is evident from Figure 1~~b~~ (b) that the upper flight leg at about 10.9 km is just above the dynamical tropopause. A close inspection of Fig. 1~~b~~ (b) reveals an almost constant altitude of the dynamical tropopause along the flight path without strong horizontal gradients or folds in the region of our measurements. The flat dynamical tropopause structure is mirrored by the ozone distribution from ERA5 data (not shown), which shows a rather homogeneous distribution at Θ = 330 K (approximately flight altitude) and notably also upwind the region of our measurements.

As mentioned above, a rectangular flight pattern at two different altitudes (7.9 km and 10.9 km) was chosen for the measurement of gravity waves. Here we focus on the flight legs parallel to the wind and orthogonal to the mountains of research flight FF09.

3.2 Time series analysis of FF09

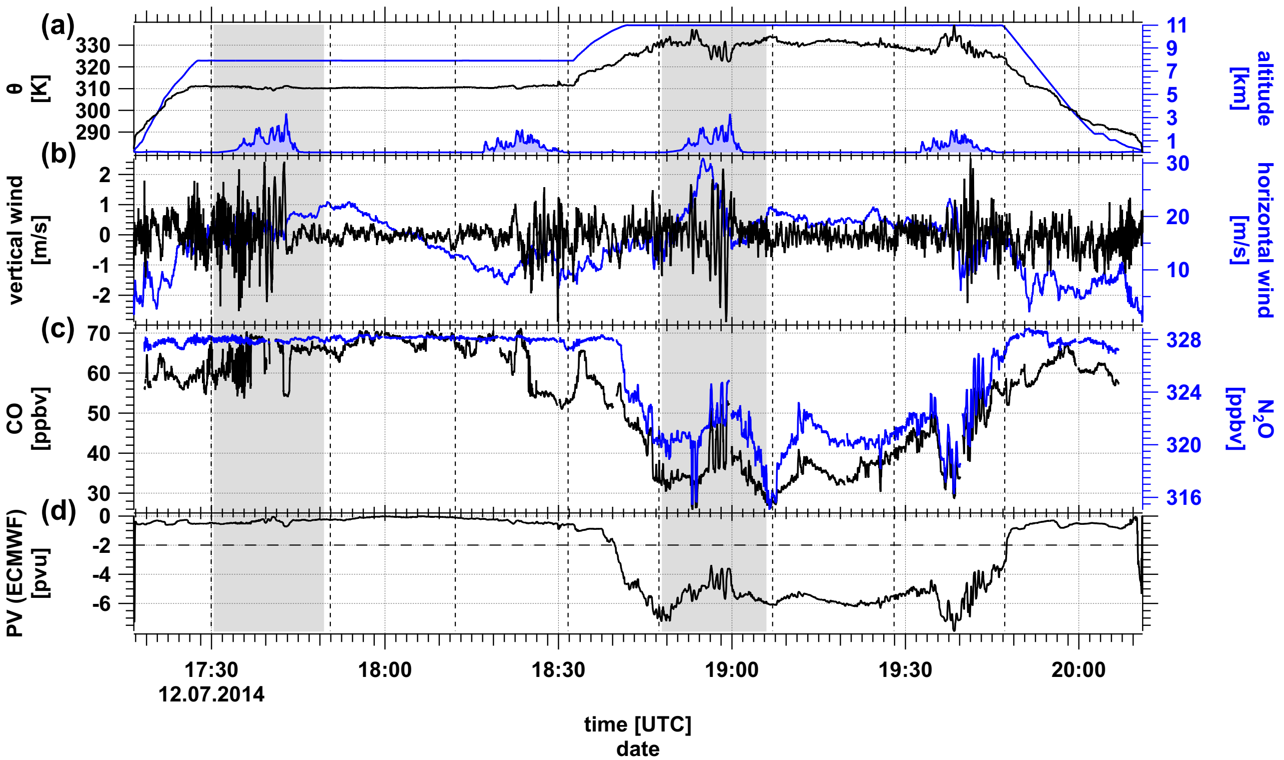

Figure 2. Time series of (a) potential temperature Θ from the measurements (black), altitude (blue) above surface elevation (filled blue), (b) vertical wind (black), horizontal wind (blue), (c) N_2O (blue) and CO (black) volume mixing ratios and (d) ECMWF potential vorticity PV interpolated along the flight track. ~~The light~~ Light gray ~~box indicates~~ boxes indicating the tropospheric and stratospheric flight section for the detailed mixing analysis. Vertical dashed lines mark turning points of the aircraft. Surface elevation was interpolated from SRTM15+ data (Tozer et al., 2019).

During flight FF09 on 12. July 2014 the flight legs were almost parallel to the horizontal wind and directed almost perpendicular to the Southern Alps. Pronounced fluctuations of the vertical wind occurred above the Southern Alps at each flight leg crossing the mountain ridge (Fig. 2).

The tropopause was crossed around 18:40 UTC, as indicated by the sharp decrease of the N_2O volume mixing ratio and the ~~analysed PV .~~ analyzed PV interpolated along the flight path. Particularly, in the regions of strong variability of the vertical wind also Θ, N_2O and CO show enhanced variability and strong fluctuations during the stratospheric part of the flight. The fluctuations of ~~potential temperature~~ Θ reached an amplitude of $\Delta\Theta = 9$ K (Fig. 2). Corresponding oscillations of the vertical wind velocity reached 5 m/s peak to peak with associated variability of N_2O on the order of 4 ppbv mirroring the oscillations of potential temperature during both flight sections parallel to the wind. These features occurred above the mountains where the meteorological analysis shows a slight altitude variability of the dynamical tropopause (~~2~~-2 pvu, Fig. 1).

3.3 Orographic waves during FF09

The flight sections of the two southern legs ~~where~~ were strongly affected by orographic waves (Fig. 3). Both legs show strong fluctuations of the vertical wind component w and the potential temperature Θ with amplitudes of ~~± 2~~2.5 ms^{-1} and 4.5 K, respectively. The passive tracer nitrous oxide (${N_2O}$~~, which has a lifetime of 110 years in the lower stratosphere,~~) indicates corresponding fluctuations at the upper level in the stratosphere. At the lower level N_2O shows a weak variability. Due to its virtually constant abundance in the troposphere N_2O does not show corresponding oscillations to w and Θ between 170.1°E-170.7°E. However, its variability does increase downwind the mountains similar to w and Θ, indicating the occurrence of turbulence. At the upper level such ~~a breakdown of scales~~ turbulence is not prominent, although the fluctuations of Θ, w and N_2O (Fig. 3) are indicative ~~for~~ of at least a potential kinematic flux of N_2O, ~~but~~ with only weakly pronounced small scale variability of w' (we defined the primed quantities according to Eqn. 4).

Before studying tracer transport and mixing we analyzed the dynamical properties of the orographic ~~gravity waves.~~ waves. The binned energy spectra of the vertical wind and the horizontal wind speed V_H are shown in Fig. 4 for the southern flight legs crossing the mountains. Both legs show pronounced peaks in the w-spectra at about 10 km horizontal wavelength. ~~For the lower leg higher values for the~~ The vertical turbulent kinetic energy ~~occurred (as given by the squared variance of the vertical wind $\overline{w'^2} = 0.70$~~was larger in the lower leg ($\overline{w'^2} = 0.70$ m^2 s^{-2}) than in the upper leg ($\overline{w'^2} = 0.53$ m^2 s^{-2}~~,~~), where the overline denotes the average over the whole 200 km ~~long flight leg) compared to the upper leg ($\overline{w'^2} = 0.53$ m^2 s^{-2})~~flight leg. However, ~~this energy~~ the energy of the lower leg seems to reside in scales smaller than about 1 km. Therefore, the spectral amplitude associated with the mountain waves at horizontal wavelengths of $\lambda_x = 10$ km is smaller at the lower leg, whereas at the upper leg wave motions with $\lambda_x \approx 10$ km dominate. No vertical energy is found at larger scales in both legs.

The situation is different for the horizontal wind spectra where the energy is at longer horizontal scales. Only the upper leg shows a spectral peak at 10 km similar to the one in w. Thus, there are two distinct gravity wave modes: one with a long horizontal wavelength (also partly seen in V_H in Fig. 2 around 17:45 UTC) that is a response to the airflow over the whole mountain range and one with $\lambda_x \approx 10$ km. The long mode is totally absent in the lower leg and corresponds well to the rather uniform horizontal wind as shown in Fig. 2 (17:30-17:50 UTC). Probably this long mode was not fully captured by the limited lengths of the legs as flown by the DLR Falcon. The other, shorter mode in the horizontal wind spectra is well-developed only in the ~~upper~~ lower leg. However, the increase of the spectral variance from the lower leg to the upper leg by a factor of seven from 1.88 m^2 s^{-2} to 13.78 m^2 s^{-2} must be mainly related to the long wave observed there according to Fig. 4.

The downstream regions of the lower leg show increased variances of the vertical wind w' at short horizontal wavelengths. ~~This~~ These enhanced variances might be related to the increase of small-scale energy as can be seen in the spectra shown in

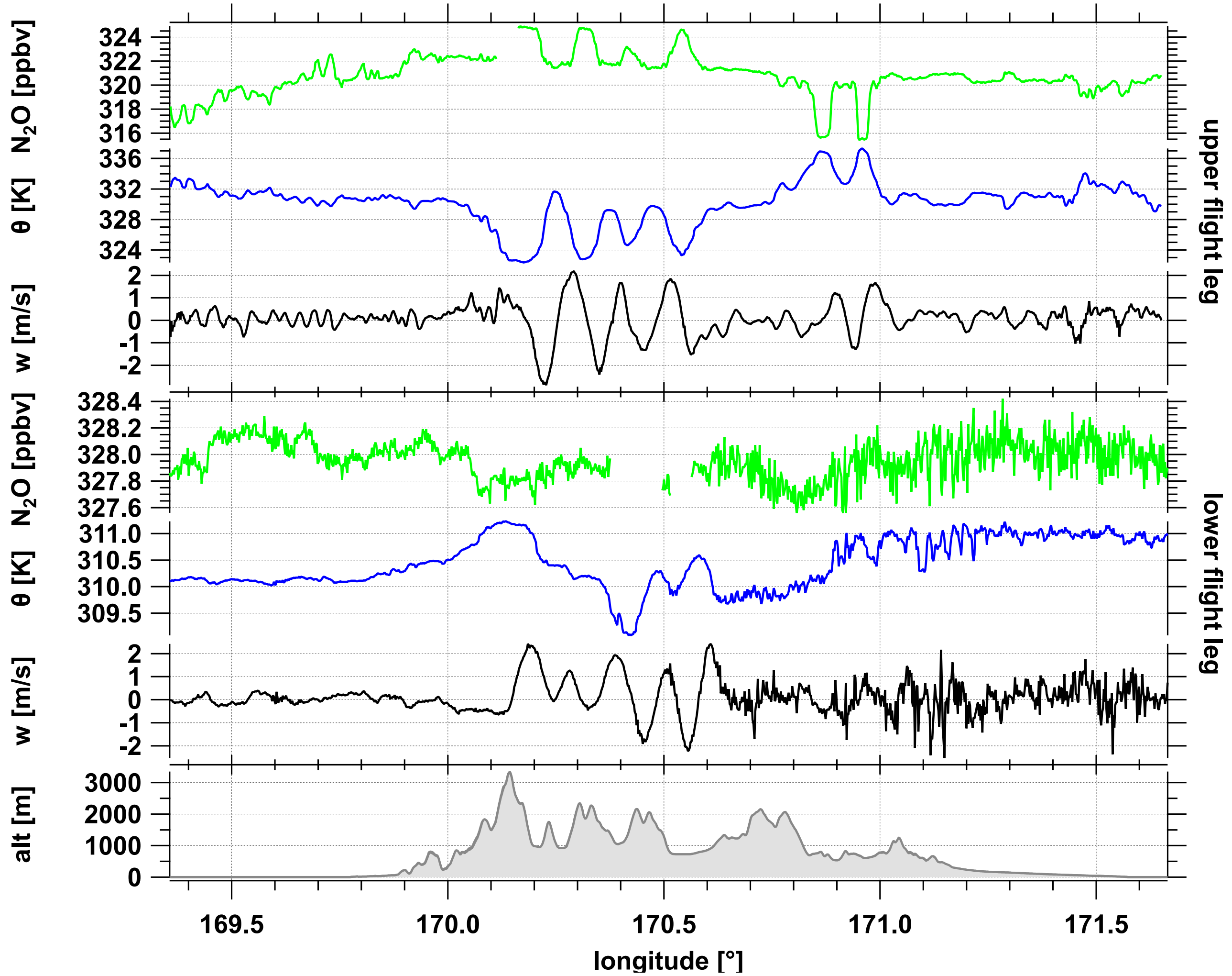

Figure 3. Cross section of the two southern stacked flight legs crossing the Southern Alps (gray shaded regions of Fig. 2) showing N_2O (green), Θ (blue) and vertical wind w (black) for the upper leg at 10.9 km (top three panels) and the lower leg at 7.9 km with surface elevation (bottom). Both legs are separated by 75 minutes in time. The upper leg lies in the lower stratosphere just above the tropopause, the lower leg lies in the upper troposphere~~just below the tropopause~~.

Fig. 4. The specific zonal momentum fluxes $\overline{u'w'}$ (Tab. 1) are negative above the mountains and their magnitude is much larger than up- and downstream. This indicates a vertical upward transport of negative horizontal momentum that is characteristic of vertically propagating mountain waves.

An estimate of the vertical momentum flux divergence based on the values from the stacked flight legs

$$-\frac{1}{\rho}\frac{\partial}{\partial z}\overline{\rho u'w'} \approx -\frac{\partial}{\partial z}\overline{u'w'} = \frac{\partial u}{\partial t} \tag{3}$$

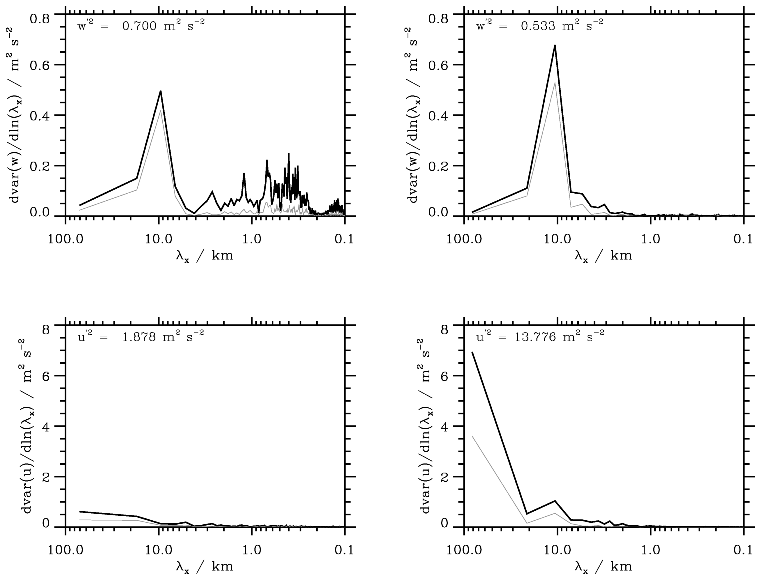

Figure 4. Binned energy spectra for the vertical ~~horizontal~~ wind component w (top row) and the horizontal wind V_H (bottom row) from the two southern flight legs of FF09, which crossed the mountains based on the 10 Hz data (corresponding to flight segments from 17:30-17:50, and 18:47-19:07 in Fig. 2). The left column shows the lower tropospheric flight track. Thick black lines are results without tapering window, thin black lines are spectra tapered with a Hanning window.

yields a deceleration of the zonal flow $\partial u/\partial t$ of about 6 m s^{-1} d^{-1}. This indicates momentum deposition by dissipating mountain waves most likely occurring in the layer between the lower leg and the upper leg. The slowdown does not seem to affect the wave-induced increase of horizontal wind in the upper flight leg. Thus, the momentum dissipation must have occurred between the two flight segments separated vertically by 3000 m. This argument is supported by the small-scale signatures found in all wind components downstream of the coherent waves in the lower leg (see Fig. 2 and Fig. 3). They indicate turbulent modes associated with local instabilities above this level.

The meridional momentum fluxes $\overline{v'w'}$ are much smaller than $\overline{u'w'}$ (Tab. 1) and will not be considered here. The zonal wave energy fluxes $\overline{u'p'}$ are negative in all segments of both legs (Tab. 1) and their magnitudes are largest directly over the mountains. Together with the positive vertical wave energy flux $\overline{w'p'}$ this finding suggests vertically propagating mountain waves that travel against the mean flow, therefore, $\overline{u'p'}$ <0.

It is interesting to note that the vertical wave energy flux $\overline{w'p'}$ decreases with height by a factor of four, which means that the waves are attenuated as they propagate from the lower leg to the upper leg. This supports the idea that dissipation must have occurred in the layer between 7.9 km and 10.9 km altitude. Vertical and horizontal wave energy fluxes are drastically reduced in the up- and downstream segments indicating no significant vertical wave propagation there.

	tropospheric leg			stratospheric leg		
	upstream	mountain	downstream	upstream	mountain	downstream
~~$\overline{u'w'}$~~ $\overline{u'w'}$ / m^2s^{-2}	0.02	-0.37	-0.18	-0.01	-0.16	0.02
~~$\overline{v'w'}$~~ $\overline{v'w'}$ / m^2s^{-2}	0.00	-0.21	0.09	0.01	0.02	-0.02
~~$\overline{u'p'}$~~ $\overline{u'p'}$ / Wm^{-2}	-0.24	-12.48	-8.72	-0.89	-24.80	-1.52
~~$\overline{v'p'}$~~ $\overline{v'p'}$ / Wm^{-2}	0.32	7.08	4.91	0.24	3.28	0.84
~~$\overline{w'p'}$~~ $\overline{w'p'}$ / Wm^{-2}	0.04	4.17	0.07	0.04	1.08	0.02

Table 1. Wave momentum and wave energy fluxes for the two southern legs separated in upstream, downstream and across mountain ~~legs~~ side according to Fig. 6.

3.4 Observation of mixing

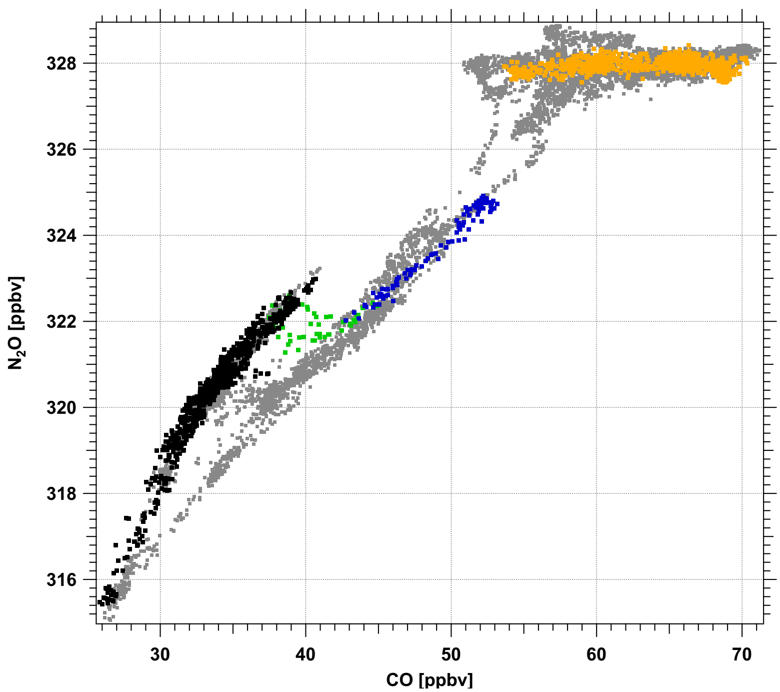

Figure 5. Scatterplot of N_2O versus CO for FF09 on 12 July 2014. The light gray points show the correlation of N_2O and CO for the whole flight. ~~Colored data points denote~~ For the upper south-western flight leg from 18:48 UTC to 19:06 UTC in Figure 2 (also compare Fig. 6) the data points are black, blue and green. Black colors indicate potential temperatures $\Theta > 328.1$ K, blue for $\Theta < 326.3$ K. The region between these two levels is marked in green. The lower leg lies entirely in the troposphere as indicated by the ~~the dark gray~~ orange data points of $N_2O = 328$ ppbv.

We use tracer-tracer scatter plots of CO and N_2O to investigate if mixing occurred in the region of the enhanced wave activity. Since N_2O has no chemical sink in the atmosphere below 25 km and a lifetime of 110 years in the lower stratosphere, it is virtually homogeneously distributed in the troposphere, but exhibits a weak vertical gradient in the stratosphere (Müller et al., 2015). In contrast, CO has a chemical lifetime on the order of weeks to months in the tropopause region. Thus, it shows a sharper gradient at the tropopause. Particularly, in the absence of mixing from the troposphere CO would fall to volume mixing ratios of 10-15 ppbv given by the balance of CO production from methane oxidation and faster CO degradation by OH. Any higher value is inevitably linked to a contribution of tropospheric air. Therefore mixing, in the sense of irreversible tracer transfer, can be detected by comparing CO to any long-lived tracer with a stratospheric gradient. The approach has been extensively used to detect tropospheric influence in the stratosphere by using CO and ozone (O_3) (e.g. Hoor et al., 2002; Zahn and Brenninkmeijer, 2003; Pan et al., 2004). Here we use N_2O instead of O_3, since it is purely controlled by atmospheric dynamics in the lower stratosphere due to the absence of local photochemical sources and sinks.

The scatter plot of CO versus N_2O for both southwesterly legs of FF09 is shown in Fig. 5. The orographic waves at the lower leg appear at almost constant N_2O ~~levels~~ volume mixing ratios of 328 ppbv. This is due to the fact, that in the troposphere no gradients of N_2O are present. Thus mixing does not change the N_2O volume mixing ratio as long as no stratospheric air is involved. Thus we cannot diagnose mixing for the lower leg on the basis of tracer-tracer correlations.

However, for the stratospheric legs across the mountain ridge during FF09 the scatter plot clearly shows different chemical regimes in the stratosphere (i.e. for N_2O < 326 ppbv, Fig. 5) as indicated by the two different branches of the two tracers. These two branches indicate two distinct air masses within the lower stratosphere which differ in their chemical composition as evident by the different N_2O volume mixing ratios. A detailed analysis (see Fig. 6) shows that the two branches of the correlation can be assigned to two distinct potential temperature intervals which correspond to two layers of different chemical composition for $\Theta > 328.1$ K and $\Theta < 326.3$ K. Notably, the data points ~~which fall inbetween the two compact relations~~ (marked in green) which fall between the two data clouds (N_2O < 324 ppbv) forming two compact branches (and thus isentropes as given above) connect both air masses. ~~They~~ The intermediate points thus mark a layer between ~~$\Theta <$~~326.3 K ~~328.1 Kand $\Theta > 326.3$~~$< \Theta < 328.1$ K, where the tracer-tracer diagram indicates mixing between the two branches (green ~~crosses~~ squares in Fig. 5).

To put the stratospheric part (i.e. for N_2O< 327 ppbv) of the tracer-tracer data of the scatter plot in a geophysical and meteorological context, Fig. 6 shows the time series of potential temperature and N_2O color coded according to the regimes identified from the scatter-plot (Fig. 5). The two branches of the correlation can be clearly assigned to different isentropes separating air masses with different chemical composition. Notably those points which indicate mixing in the tracer-tracer scatter plot fall ~~inbetween~~ between the distinct layers. As evident from Fig. 6 the region where the chemical composition indicates mixing (green) corresponds to the occurrence of waves as indicated by strong fluctuations of the vertical wind and potential temperature. Therefore we hypothesize that mountain wave induced mixing must have occurred in the stratosphere leading to the observed tracer variability as shown above. In the following we will therefore focus on the stratospheric flight section across the mountains from 18:48 UTC to 19:06 UTC as indicated by the gray box in Fig. 2 if not noted differently.

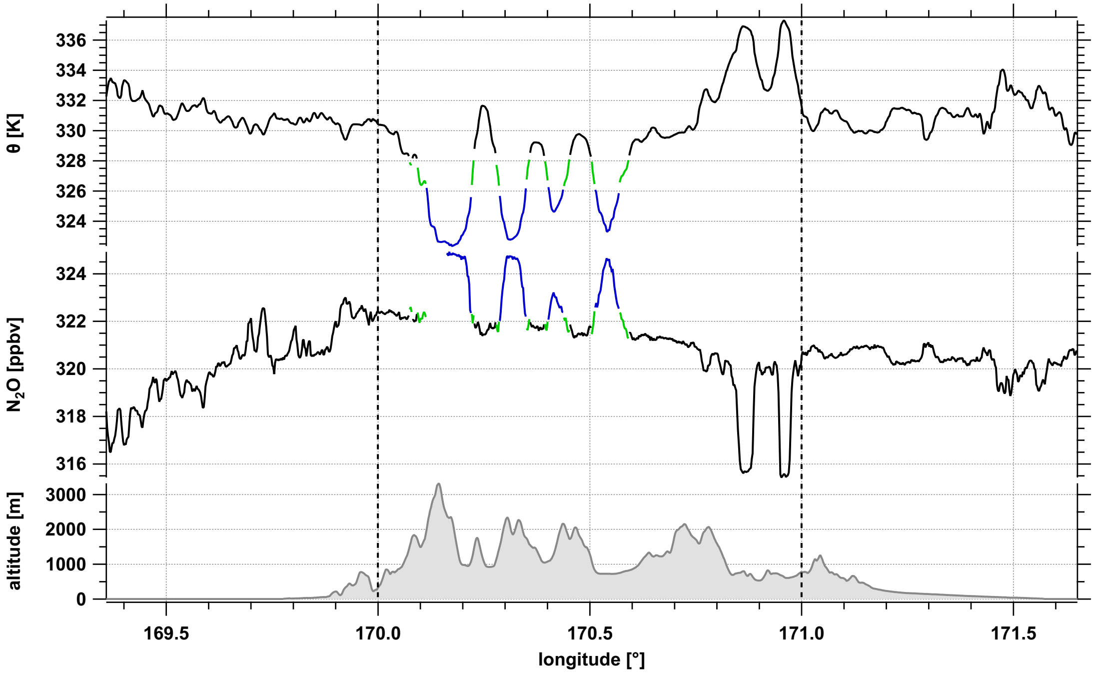

Figure 6. Time series of potential temperature Θ and N_2O for the flight leg around 18:48-19:00 UTC just above the tropopause over the mountain. ~~Colours~~ Colors indicate two different layers of air masses (black, blue) and a mixed layer ~~inbetween~~ between (green) corresponding to Fig. ~~??~~5. Vertical lines mark the upstream (<170°E), above mountain (170°E-171°E), and downstream side (>171°E).

4 Analysis of cross-isentropic mixing

Kinematic fluxes on the basis of the covariance of vertical wind and tracer variability $w'\chi'$ might provide information on the local vertical fluxes. For a correct estimate of an irreversible flux one needs to calculate the flux divergence (Shapiro, 1980). However, this would require simultaneous measurements of the tracer of interest on two ~~vertically closely stacked~~ closely stacked vertical levels, which ~~can not~~ cannot be accomplished with one aircraft (as was the case here). A comparison of the local fluxes for the stacked levels is in principle possible. However, due to the large vertical spacing of 3 km, the potential influence from large scale horizontal advection could strongly impact the flux divergence estimates between the two flight levels.

Adiabatic vertical displacements of air masses may simultaneously displace the location of isentropes and tracer isopleths, which therefore does not lead to irreversible tracer transport and mixing at a given location downwind of a mountain ridge (i.e. $\partial\chi/\partial\Theta = const$, Moustaoui et al. (2010)). In contrast, cross-isentropic (= diabatic) fluxes must change cross-isentropic gradients of species (i.e. $\partial\chi/\partial\Theta$) with respect to potential temperature. Therefore, a change of tracer ~~slope~~ gradient (i.e. ~~gradients~~ $\partial N_2O/\partial\Theta$) as a function of Θ downwind the mountain is indicative for irreversible cross-isentropic tracer exchange which might have occurred above the mountain ridge. In a Lagrangian sense the occurrence of turbulence and turbulent mixing acts as a source of tracer at a given isentrope, if the background tracer gradient changes with height in the inflow region (like e.g. at the tropopause). We therefore investigated if tracer gradients with respect to potential temperature Θ were changed due to the occurrence of gravity wave induced ~~turbulent~~ turbulence leading to cross-isentropic mixing by comparing local tracer profiles upstream and downstream the mountains ($\partial\chi/\partial\Theta|_{up} \neq \partial\chi/\partial\Theta|_{down}$).

In particular, the gradient change of the conservative tracer N_2O at the tropopause is perfectly suited to test our hypothesis ~~.~~ that gravity wave-induced turbulence lead to cross-isentropic mixing. Since N_2O ~~at the tropopause~~ in the lowermost stratosphere is not affected by local chemistry it is purely under dynamical control. At the tropopause, N_2O exhibits a change of the vertical gradient ~~and as a function of~~ with respect to Θ ($\partial N_2O/\partial\Theta$).

The decrease of N_2O in the lowermost stratosphere with respect to Θ is schematically shown in Fig. 7. For the following analysis we will use the following conventions: we will express the slope as ratio of the anomalies Θ'/N_2O' (according to Eqn. 4) to be consistent with the profile view (as in Fig. ~~6). Thus, mixing across the tropopause, e.g. via gravity wave induced turbulence may lead to a change of the~~ 7 and Fig. 8). We will apply this convention with Θ in the numerator and N_2O ~~profile relative~~ in the denominator throughout the following analyses below. We will further use the following terminology:

The term Θ-N_2O-relation refers to general aspects of their relation, the term Θ'/N_2O'-ratio (associated with a slope) will be used when referring to the specific measurements further below. A change of this ratio is directly linked to the change of the vertical gradient with respect to Θ ~~.~~ ($\partial N_2O/\partial\Theta$).

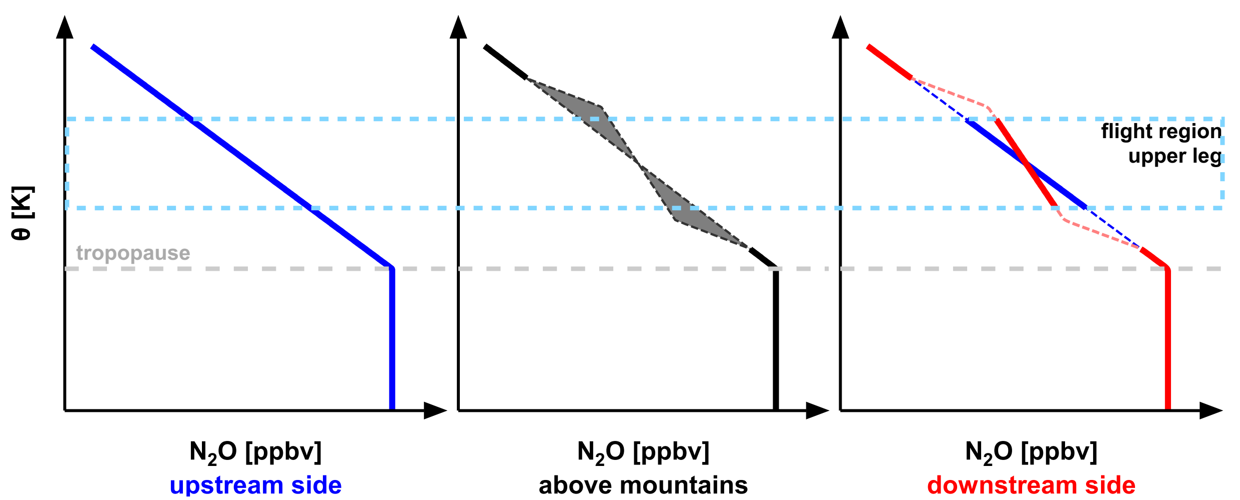

Figure 7. Schematic evolution of ~~versus~~ potential temperature Θ versus N_2O in the presence of cross-isentropic mixing (indicated by the ~~grey~~ gray arrows) at the tropopause (e.g. by orographic wave-induced turbulence)~~, which changes the potential temperature gradient~~. The blue curve (left panel) shows the situation on the upstream side. The relation ~~of~~ between N_2O and Θ (blue) is modified by mixing (dotted black and ~~grey~~ gray shaded) over the mountains leading to a modified profile on the downstream side (red) compared to the original upstream relation (blue). The ~~grey~~ gray dashed line shows the tropopause and the light blue dash rectangle the flight region of the upper leg.

~~This is schematically~~ A schematic of our hypothesized relation of Θ and N_2O is shown in Fig. 7 ~~,~~ which shows the evolution of the N_2O ~~-Θ~~ profile for a flow over a mountain assuming an effect of gravity wave induced cross-isentropic mixing on the N_2O profile. The upstream side represents the unperturbed background N_2O profile. Above the mountain orographic wave induced turbulence may occur which could potentially change the ~~cross isentropic~~ vertical gradient of N_2O ~~relative to potential temperature~~ ~~$\partial N_2O/\partial\Theta$~~ with respect to Θ at the tropopause. This effect of irreversible mixing is schematically depicted by the gray shading in Fig. 7. Since ~~the -gradient~~ $\partial N_2O/\partial\Theta$ changes at the tropopause the upstream relation between Θ and N_2O can be modified by turbulent mixing ~~and~~ which will change the relation of the N_2O ~~-Θ profile changes~~profile with respect to Θ. As a result of the irreversible diabatic process the downstream side shows the modified profile of N_2O ~~versus Θ~~ compared to the upstream region (red versus blue ~~slopes~~slope).

Thus, in case of gravity wave induced turbulent mixing during flight FF09, we expect a ~~steeper vertical~~ more rapid decrease of N_2O ~~-~~with increasing Θ ~~gradient~~ in the inflow region upwind the mountains ~~(i.e. a smaller Θ' ' ratio)~~ than at the downstream side of the mountain ridge as an effect of turbulent mixing. The vertical N_2O profile with respect to Θ is modified from upstream to downstream due to turbulent mixing.

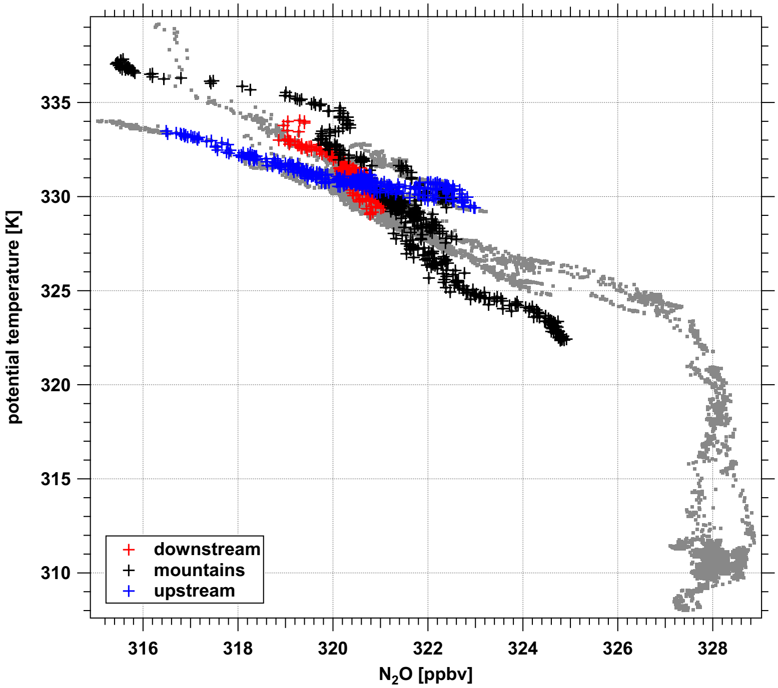

Figure 8. Profile of N_2O during FF09 (gray) as a function of potential temperature Θ. The upper leg of the southwestern part is shown with different colors, indicating different flight sections along the flight leg (blue: upstream, red: downstream, black: above the mountains, comp. Fig. 6).

~~Figure~~ Figure 8 shows the measured N_2O profile as a function of potential temperature Θ for the entire flight FF09. The colored data points denote different longitudes relative to the mountain ridge to separate the inflow, across mountain, and downstream part of the flight leg ~~between 170°E-171°E~~ (see Fig. 6). As evident from Fig. 8 different ~~slopes of versus~~ relations between Θ and N_2O appear on the upstream side, downstream side and above the mountains~~corresponding to the hypothesis described above. The~~. The different relations are consistent with our hypothesis that the relationship between Θ and N_2O ~~-~~(and consequently the vertical gradient $\partial N_2O/\partial\Theta$) will be changed in regions impacted by gravity wave induced mixing. Upstream of the mountains this Θ~~-slope on the upstream side~~-N_2O-relation shows a strong decrease of N_2O with ~~potential temperature~~ increasing Θ and a compact relationship (i.e. a well defined relationship exhibiting only weak scatter). On the downstream side the N_2O decrease with respect to Θ is much weaker with intermediate values and larger variability above the mountains (see Fig. 8).

4.1 Scale analysis

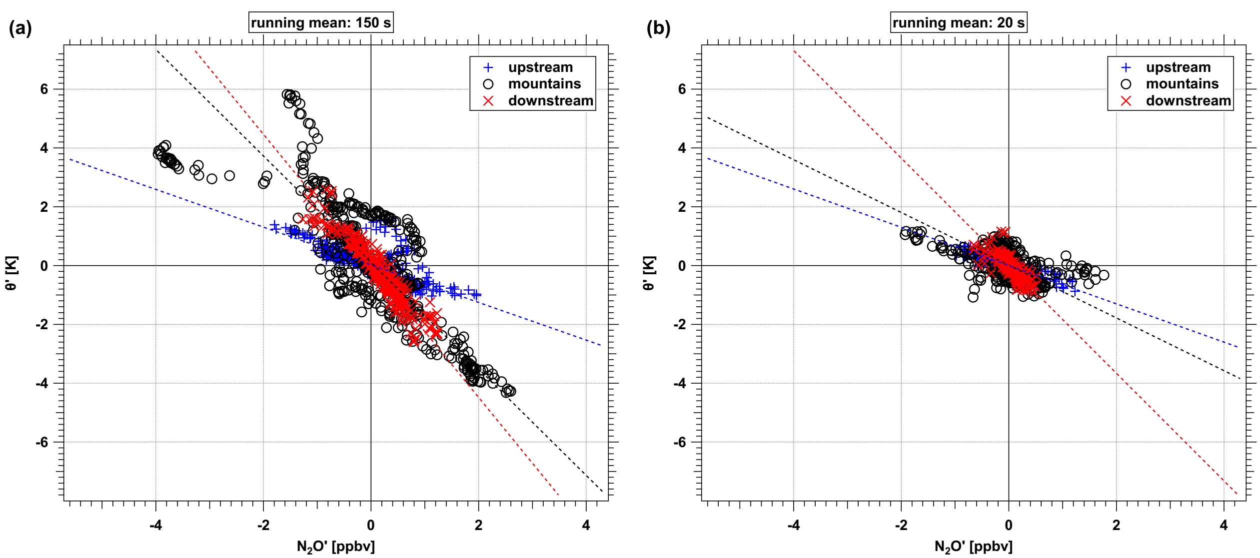

Figure 9. ~~Relationship~~ Relation between ~~Θ'~~ Θ' and N_2O~~i'~~$'$ for upstream (blue), downstream region (red) and above mountains (black). Left: averaging period of 150 s (32.5 km). Right: averaging period of 20 s (4.3 km). The dotted lines indicate the slopes of the different flight segments. Note the changing slope over the mountains.

In a next step we performed a scale dependent correlation analysis as described below to further ~~analyse~~ analyze the impact of the orographic waves on the ~~-~~Θ-N_2O relation and to account for a potential effect of different scales of the waves on cross-isentropic mixing. For this, we applied a Reynolds decomposition and separated the data into a mean part $\overline{\chi}$ and a perturbation part ~~χ'~~ χ' (as well as ~~Θ and Θ').~~ $\overline{\Theta}$ and Θ').

$$\chi(t) = \overline{\chi} + \chi''(t) \Leftrightarrow \chi''(t) = \chi(t) - \overline{\chi} \tag{4}$$

The mean $\overline{\chi}$ is calculated with a boxcar average which works as a low-pass filter and removes high frequency variability. ~~As given in detail further below, we analysed~~ We analyzed the data for different averaging periods to account for varying perturbation ~~wave lengths and to analyse the effect~~ wavelengths and at different scales ~~.~~ using the formula:

$$\overline{\chi} = \frac{1}{t_2 - t_1} \int_{t_1}^{t_2} \chi(t)\, dt \tag{5}$$

where $t_2 - t_1$ is the integration width.

Above the tropopause Θ increases while N_2O ~~$'$ and Θ' are linearly correlated with a particular slope defined by the upstream conditions~~decreases. Thus, we expect an anti-correlation for the perturbations of these two quantities, Θ' and N_2O' with a given slope (or Θ'/N_2O'-ratio) in the inflow region upstream of the mountains. For linear non-dissipative waves the ~~relation between $'$ relative to Θ'~~ Θ'/N_2O'-ratio will therefore remain constant for different integration widths. In the presence of non-conservative dissipative processes the linear relation between Θ' and N_2O' ~~-Θ'~~ and thus their ~~slope~~ ratio will change as explained above.

As an example the effect of different integration intervals on the distribution of data points is shown in Fig. 9 for two different interval lengths. The applied fit accounts for errors in x and y direction (Press et al., 1987). The Figure shows the same subset of data using averaging periods on display of 150 s (Fig. 9 ~~a)~~(a)) and 20 s (Fig. 9 ~~b)~~(b)) corresponding to a horizontal scale of 33 km and 4 km, respectively. For wavelengths shorter than these dimensions the ~~slopes~~ ratios at the downstream (red) and upstream (blue) side only slightly change. Both however clearly show an increased ~~slope~~ ratio at the downstream side (red) compared to the upstream (blue).

Above the mountains (black) the relation is perturbed, showing a high variability. The above ~~mountain-slope~~ mountain-ratio for the long waves (i.e. averaging periods, left panel) is closer to the downstream side compared to the shorter wavelengths (right panel).

To account for different scales and thus increasing wavelengths, we subsequently increased the averaging period in steps of one second from 2 - ~~512 s~~ 292 s (length of the shortest data segment unbroken by calibrations). The corresponding development of the ~~slopes between $'$ and Θ'~~ Θ'/N_2O'-ratios is shown in Fig. 10. The blue curve is deduced from the data in the upstream region. With a value of about 0.6 K/ppbv the ~~slope~~ ratio is almost constant over all averaging periods. This indicates that no cross-isentropic mixing perturbs the ~~linear $'$-Θ' relationship~~ upstream linear Θ'/N_2O'-ratio at any wave period.

Indeed in the long scale limit a clear separation for the downstream and above-mountain ~~slope~~ ratio is evident. The black and red curves show a ~~slope~~ Θ'/N_2O'-ratio change for different averaging periods. Above the mountains the ~~slope~~ Θ'/N_2O'-ratio starts to change at longer averaging periods (100 s, 21.6 km) compared to the downstream side. The changes at the downstream side start at shorter averaging periods (40 s, 8.7 km) indicating smaller scales or wavelengths relevant for the change of the

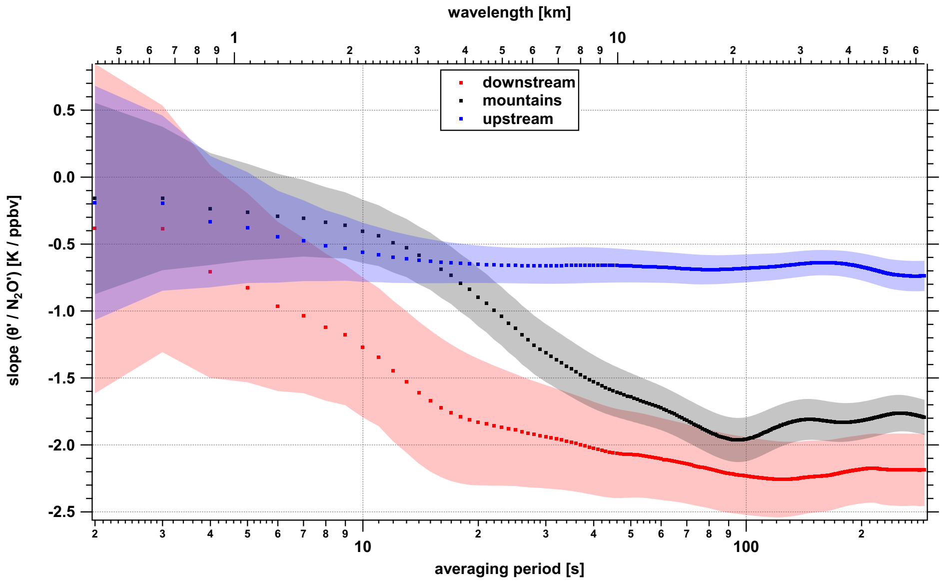

Figure 10. Scale dependent correlation anomaly analysis for different integration times showing the ~~slope between ′ and Θ′~~ Θ'/N_2O'-ratio for different averaging periods (i.e. wavelengths) for upstream (blue), ~~lee~~ downstream (red) and above mountains (black).

Θ'/N_2O'~~-Θ'-relationship~~-ratio. Downstream and above-mountain ~~slopes~~ Θ'/N_2O'-ratios merge for longer periods to the new (modified) gradient with a ~~slope~~ Θ'/N_2O'-ratio around 2 K/ppbv.

Similar to Alexander and Pfister (1995) we used the upstream relation ~~of~~ between Θ ~~/~~and N_2O to estimate the N_2O amplitude which one would expect if only adiabatic transport by the gravity waves over the mountain would occur. The observed peak-to-peak variability of Θ ~~-amplitude~~ of 8 K (Fig. 6) would correspond to N_2O = 13 ppbv, while only 4 ppbv are observed consistent with an impact of diabatic mixing processes changing the upstream relation.

In summary the ~~slope changing behaviour~~ ratio changing behavior would be consistent with a modification of the initial upstream N_2O-~~Θ~~-profile across the mountains, where the relation between ~~and~~ Θ and N_2O is perturbed. When crossing the mountain ridge gravity wave induced turbulence affects the ~~-~~Θ-N_2O-relation with a persistent effect at the downstream side. ~~This~~ The downstream impact is evident from the different ~~′-Θ′ slope at larger wave lengths at the lee~~ Θ'/N_2O'-ratio at larger wavelengths at the downwind side compared to the upstream ~~slope~~ratio. Therefore we conclude that during FF09 mountain waves modified the ~~slope -Θ~~ Θ'/N_2O'-ratio by the generation of turbulence at small scales~~and~~. They induced cross-isentropic turbulent mixing leading to changes at large scales downwind the Alps as evident from the Θ'/N_2O'-ratio and finally the vertical gradient $\partial N_2O/\partial \Theta$ (Fig. 6).

To identify the leading spatial and temporal scales for the cross-isentropic (i.e. irreversible) mixing of N_2O we analyzed the wavelet coherence between the time series of N_2O and Θ in Fig. 11. Coherence is a measure of the intensity of the covariance of two time series. At the upstream side (< 170°E) there is mostly high coherence according to the fact that Θ and N_2O co-

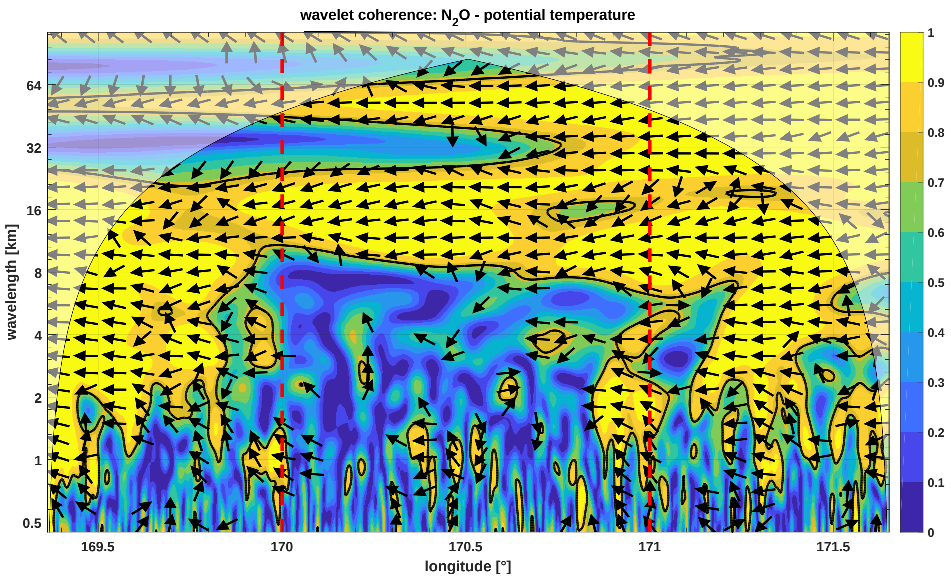

Figure 11. Wavelet coherence of N_2O and potential temperature (wavelength = period · flight speed (216 m/s), see Eqn. 2). Arrows to the left indicate that N_2O and potential temperature are shifted by 180°. In regions with a coherence lower than 0.5 the phase indication is removed. The shaded region marks the cone of influence, where edge effects affect the analysis. The solid lines shows the ~~5~~95 % ~~significance~~ confidence level as given in paragraph 2.4. Yellow colors indicate a high coherence and blue colors indicate a low coherence. Vertical lines mark the upstream, above mountain, and downstream side.

vary across different time scales from 1.7-17.3 km (corresponding to 8-80 s). Further, the phase relation ~~is~~ between the time series of N_2O and Θ (see Fig. 6) is almost constant at 180° for scales < 20 km, which one would expect for ~~a decreasing vertical~~ opposing vertical gradients of N_2O ~~gradient~~ and Θ in the stratosphere~~, but increasing Θ~~. Thus, both ~~findings confirm the conclusion~~ the wavelet coherence and the phase relation confirm the finding of the absence of mixing from the previous upwind slope analysis (Fig. 10, upstream side).

Above the mountains (from 170°E to 171°E) there is low coherence with values lower than 0.7 for time scales < 8,7 km (< 40 s) accompanied by a breakdown of the phase relation ~~of~~ between N_2O and Θ, both indicating a decrease of the covariance. On the downstream side (from 171°E) especially at small periods higher coherence values and defined phase ~~transitions appear~~ relations re-establish compared to the above-mountain regime, albeit more variable than at the upstream side. ~~This matches roughly the results seen in~~ Consistent with Fig. 10~~. In~~ , in upwind regimes with a high coherence N_2O and the potential temperature Θ co-vary~~. The~~ ; the phase relation between them remains constant across scales and the calculated slope (Fig. 10) is unchanged too. Above the mountains the phase relation breaks down due to cross-isentropic mixing especially for wave periods smaller than 6.5 km (30 s). Downwind a new ~~slope relation~~ ratio reestablishes as a result of mixing above the mountain ridge, but with a defined phase relation again, but different ~~slopes~~ratios.

We therefore conclude that ~~for wave periods with~~ above the mountains the low coherence and the breakdown of the phase

~~above the mountains the relationship between and Θ~~ relationship at short wavelength were an effect of the gravity waves which produced turbulence and led to cross-isentropic mixing. Therefore, the change in the Θ'/N_2O'-ratio from the upwind to the downwind side is the result of gravity wave induced mixing~~leading to the observed -Θ slope change~~. Since the mixing is cross-isentropic this changed the Θ'/N_2O'-ratio, which is evident at the downstream side, where a modified ~~slope relation establishes~~ ratio establishes (compared to the upwind side).

4.2 Fluxes

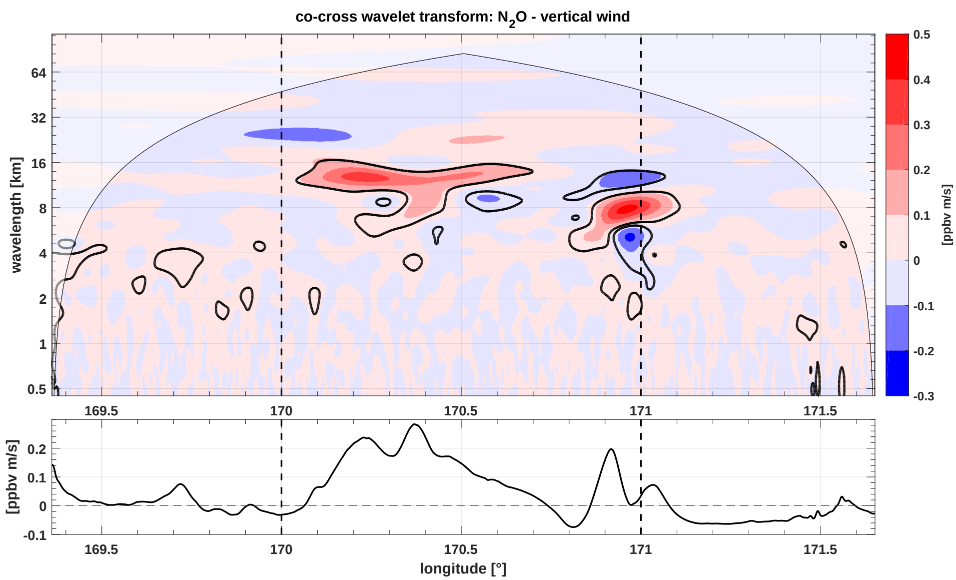

Figure 12. Top: Co-spectrum of the cross wavelet transformation of N_2O and vertical wind. The shaded region marks the cone of influence in which edge effects play a role. The black contour lines indicate 5% significance levels against red noise. Red colors ~~denotes~~ denote a positive flux and blue colors indicate a negative flux. Bottom: Scale-averaged wavelet co-spectrum over all periods.

To estimate quantitative tracer fluxes we use the co-spectrum of the cross wavelet transformation between the vertical wind w and N_2O (see section 2.4). Unlike other methods the wavelet analysis has the advantage to resolve wave induced processes in space and time.

The wavelet co-spectrum is calculated from the real part of the cross wavelet transformation and gives the spectral contributions of vertical fluxes (Mauder et al., 2007). Fig. 12 shows the co-spectrum of the cross wavelet transformation of N_2O and vertical wind w for the higher flight level during FF09. There are two regions with enhanced fluxes within the 5% significance level (black solid line), which are both located above the mountains (compare Fig. 2). The first region is between 170.0°E and 170.6°E, the second at 170.8°E and 171.0°E~~The first~~. The last region shows mainly positive trace-gas fluxes with values up to 0.50 ppbv m s^{-1} at ~~periods~~ wavelengths ranging from 8-16 km corresponding to the vertical wind energy maximum around $\lambda_x = 10$ km Fig. 4. The second region exhibits upward and downward fluxes at slightly shorter scales from about 3-16 km.

Here the strongest fluxes have values from about -0.22 to +0.56 ppbv m s^{-1}. The fluxes in both regions are co-located to enhanced wave occurrence above the mountains, as seen in Fig. 6 and Fig. 2.

Since ozone was measured with a temporal resolution of 10 s we did not directly determine ozone fluxes in the present case. To give an estimate of the associated ozone flux we can use the N_2O-O_3 correlation slope, which is about -20 ~~pppv~~ppbv (O_3) /~~ppbv~~ ppbv (N_2O) for the southern hemisphere July (Hegglin and Shepherd, 2007). This results in a negative flux of O_3 of 10 ppbv m s^{-1} for the positive N_2O-fluxes.

4.3 Turbulence occurrence

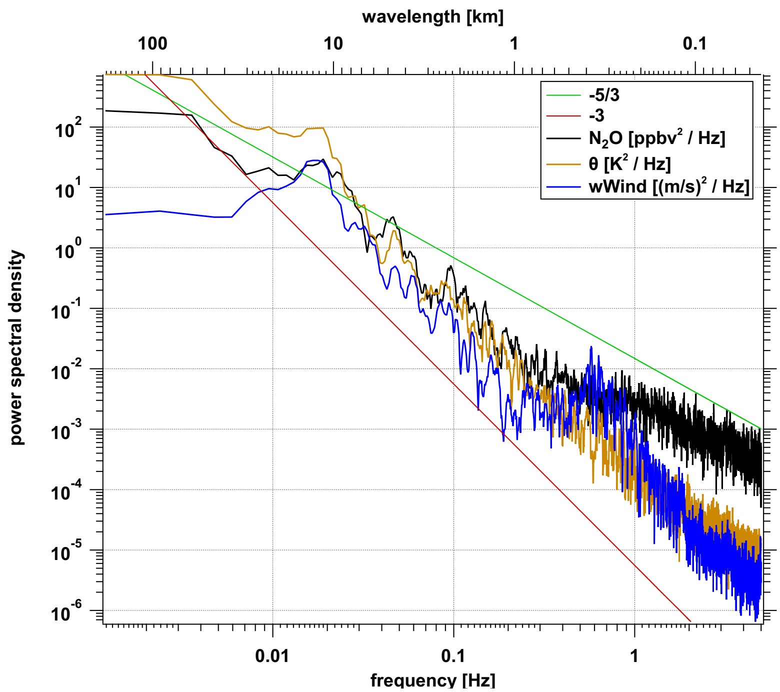

Figure 13. ~~Smoothed power~~ Power spectral density of vertical wind (blue), potential temperature (orange) and N_2O (black) for the flight ~~leg~~ segment above the mountains. The power spectral density has been smoothed by a boxcar average of 5 seconds. The green and red reference lines have slopes of -5/3 and -3.

The power spectral density (PSD) for the Θ, and the vertical wind component w in Fig. 13 shows a slope of -3 for frequencies smaller than 721 m (0.3 Hz), which is indicative for geostrophic turbulence (Zhang et al., 2015). For higher frequencies (i.e. shorter wavelengths) the increase of the power spectral density at 433 m (0.5 Hz) would be consistent with a potential source of turbulent energy above the mountains. Notably, a similar peak of the PSD of w was observed during the START08 campaign for some flight sections in regions of turbulence occurrence over the Rocky Mountains (Zhang et al., 2015). However, the peak of the PSD from the vertical wind component around 433 m (0.5 Hz) could also correspond to oscillations caused by the autopilot of the aircraft (Schumann, 2019). They report oscillations with wavelengths of 6.7 km in regions of high turbulence, which is factor of 10 longer than in our case. Thus, an artificial non-atmospheric origin of the peak cannot be completely ruled out.

The slope of the PSD of both ~~,~~ w and Θ turns towards -5/3 for frequencies exceeding 108 m (2 Hz), which can be related to isotropic turbulence. Fig. 13 also shows the PSD of N_2O which show a slope of -5/3 for frequencies smaller than 721 m (0.3 Hz) and a -5/3 slope for higher frequencies. The transition of geostrophic to isotropic turbulence as indicated by the transition of PSD-slopes occurs in the ~~frequency range~~ wavelength range between 271 m to 721 m (corresponding to 0.8 Hz to 0.3 Hz), where the PSD of the vertical wind indicates a source of turbulent energy. Notably the PSD of N_2O indicates a turbulent ~~behaviour~~ behavior for high frequencies and thus the occurrence of turbulent fluxes corresponding to the analysis in the previous section.

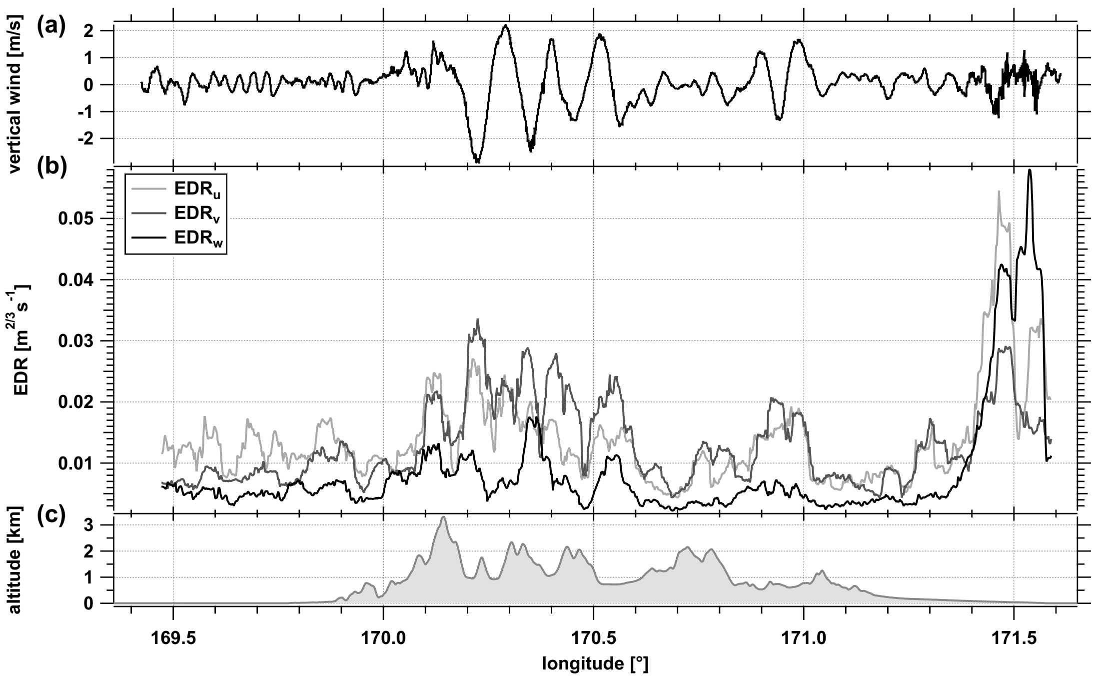

Figure 14. Timeseries of (a) vertical wind, (b) EDR for the measured wind components for the upper flight leg indicating weak, but non-vanishing turbulence during the time of flight above the Southern Alps (~~ororaphy~~ orography shown in (c)).

Further support for our hypothesis ~~and our results~~ that mountain wave induced turbulence perturbed the N_2O profile comes from the analysis of the cubic root of the eddy dissipation rate EDR = $\epsilon^{1/3}$ from the measured 3D-winds. For this analysis the we used the method by Bramberger et al. (2018) to calculate the EDR for the three wind components as measured by the aircraft (Fig. 14). Above the mountains the oscillations of the vertical wind velocity w indicate the region of mountain wave occurrence. The EDR over the mountains appears to be weak below the threshold of light turbulence of about 0.05 $m^{2/3}s^{-1}$

(Bramberger et al., 2018). However, the values of EDR~~$_{u,v}$~~$_{u,v}$ for the horizontal wind components over the mountains are similar to those of the end of the leg, ~~when also~~ where EDR$_w$ was also enhanced in the lee of the mountains.

Further support for our hypothesis and our results comes from the analysis of the occurrence of mountain wave induced turbulence using the ~~GTG (~~Graphical Turbulence Guidance ~~)~~ (GTG) using ECMWF operational analysis data (Bramberger et al., 2018; Sharman et al., 2006; Sharman and Pearson, 2017). The GTG analysis matches the observed locations of wave occurrence during the flight and the regions of strong variability of the vertical wind (not shown). Though the values are too high this supports the conclusion that turbulence occurred in the region of the mixing events either shortly before or during the measurements.

The weak EDR at the upper flight leg in accordance with the weak turbulence occurrence as opposed to the lower leg (see ~~Fif~~Fig. 4) may be explained by the time difference between the two legs. As evident from the wave analysis orographic waves were crossed during the first leg and led to wave breaking and momentum deposition in the region between the legs. At the higher leg only a weak turbulence signal remained one hour later when the second crossing took place. The change of ~~the~~ $\partial\Theta/\partial N_2O$ ~~$-\Theta$ gradient~~ is a unique indication of a diabatic process, which must have changed the gradient from the upstream to the downwind side exactly above the mountains. The evidence for strong orographic wave activity at the lower level ~~and~~ that propagating to the 10.9 km level serves as the only plausible explanation for ~~this~~ these observations. The fact that at the higher level the turbulence is weak during the time of flight must be attributed to the time shift between the two flight legs and the high intermittency of turbulence~~occurrence.~~ .

5 Conclusions

We present an analysis of high resolution N_2O measurements in the region of orographic gravity ~~wave occurrence~~ waves over the Southern Alps in New Zealand during the DEEPWAVE 2014 campaign. These gravity waves led to diabatic trace gas fluxes and a persistent local effect on the composition downwind the mountain and the above the tropopause.

The spectral analysis of the wind components measured along two vertically stacked levels indicates dissipation of momentum by orographic waves above the mountains between these levels and the generation of turbulence. The spectral energy of the vertical wind component shows strong signals at short horizontal ~~wave lengths~~ wavelengths (<1 km) at the lower flight leg at 7.9 km. At the higher leg, which was flown 75 min later in the stratosphere, horizontal ~~wave lengths~~ wavelengths of 10 km dominate the energy spectrum of w' with much weaker contribution at the shorter scale. Corresponding to the fluctuations of the vertical wind and potential temperature Θ~~also~~ , strong fluctuations of the tracer N_2O were also observed at the upper flight leg in the region of the occurrence of orographic waves. Based on the analysis of the CO-N_2O relationship we could identify mixing between two layers of different air masses in the tropopause region. Upstream and downstream of the mountain different vertical gradients of N_2O ~~versus~~ with respect to potential temperature Θ were observed and enhanced variability of this gradient was observed above the mountains. Since N_2O is chemically inert, a change of the N_2O-Θ~~relation~~ -relation must be due to cross-isentropic mixing effects.

A scale dependent slope analysis shows that mixing was initiated over the mountain ridge ~~showing~~ with reversible displacements of tracer isopleths and Θ. ~~Above the mountains these fluctuations~~ These fluctuations must have perturbed the compact ~~slope of~~ relation between Θ and N_2O ~~in the inflow region around the tropopause~~via the generation of turbulence and thus irreversible turbulent cross-isentropic mixing.

~~The behaviour~~ Mountain wave induced mixing is also consistent with the indication for wave breaking and momentum deposition above the mountains between the two flight legs. Noting that the stratospheric flight leg was flown 75 min after the lower leg explains why the turbulent kinetic energy for w' at short horizontal ~~wave lengths~~ wavelengths is rather small compared to the lower leg. Still the power spectral energy spectra of N_2O and Θ with slopes of -5/3 at the smallest scales can be seen as the result of the turbulence ~~occurring potentially previously~~ that may have occurred on this level.

The tracer distribution conserves the effect of ~~the~~ prior occurrence of highly transient turbulence occurrence. At the downstream side a modified compact N_2O-Θ~~relation~~ -relation establishes as a result of the wave induced turbulence above the mountains~~modulating the~~. The reversible air mass displacements induced by the gravity waves similar ~~as~~ to the mechanism described in (Moustaoui et al., 2010; Mahalov et al., 2011). This ~~behaviour~~ behavior is confirmed by ~~cross-wavelet~~ cross wavelet analyses showing a breakdown of the coherence and phase relationship ~~of~~ between N_2O and Θ over the mountains.

The vertical fluxes of N_2O are estimated to be 0.5 ppbv $\mathrm{m\,s^{-1}}$ corresponding to negative fluxes of O_3 of approximately 10 ppbv $\mathrm{m\,s^{-1}}$.

The change of the ~~-Θ-relationship~~ -N_2O-relation from the upstream to the downstream side over the mountain ridge is a unique indicator for cross-isentropic (i.e. irreversible) turbulent exchange of species, which was initiated by the orographic waves. The fact ~~,~~ that the modified relationship prevails downstream of the mountain shows ~~,~~ that the turbulence associated with the orographic waves was associated with cross-isentropic mixing. ~~This approach~~ The approach using the Θ-N_2O-relation notably differs from local covariance analysis of vertical winds and tracers since it shows ~~,~~ that at least part of the kinematic fluxes contributed to a cross-isentropic component.

Diabatic trace gas fluxes are key for understanding the effect of mixing processes on the large scale composition of the ~~tropopause region and the lower stratosphere~~ UTLS where they contribute to the mixing induced uncertainty of radiative forcing estimates (Riese et al., 2012). Though the occurrence of orographic waves has strong seasonality and a high degree of transience (Fritts and Alexander, 2003; Rapp et al., 2021) regions of gravity wave activity are hotspots for turbulence ~~occurrence~~ at the tropopause (Alexander and Grimsdell, 2013; Fritts and Alexander, 2003). Our data show that ~~this~~ gravity wave induced turbulence can have a persistent effect on the distribution of species and thus a potential forcing impact of radiatively active tracers by changing their isentropic gradients. By subsequent isentropic transport as part of the stratospheric flow ~~their impact~~ the impact of radiatively active traces has a strong non-local component downwind ~~contributing~~ the mountains. Thus, gravity wave induced mixing contributes to the overall mixing induced uncertainty of radiative forcing (Riese et al., 2012).

Data availability. ECMWF analysis data have been retrieved from the ECMWF MARS server. The airborne measurement data from the DEEPWAVE campaign are available through the HALO database (https://halo-db.pa.op.dlr.de/, last access: 6 June 2022).

Author contributions. PH conceived the study. HCL performed most of the data analysis with guidance from PH and DK. AD performed the gravity wave analysis. MB provided the EDR analysis. SM and PR performed the UMAQS measurements during DEEPWAVE and contributed to the flight planning. TK contributed to the turbulence analysis. AG provided the wind and turbulence data. MR and AD designed the DEEPWAVE campaign and the scientific flight planning. HCL and PH wrote the paper with contributions from DK; all authors contributed to the discussion of the results and the manuscript.

Competing interests. The authors declare that they have no competing interests.

Acknowledgements. The project was funded by the Deutsche Forschungsgemeinschaft (DFG) under grant HO 4225/6-1. The authors acknowledge support by the German Aerospace Center (DLR) Oberpfaffenhofen. The authors gratefully acknowledge support by the SFB/TR-301 (TPChange: The Tropopause Region in a changing atmosphere, Project-ID 428312742). Part of this research was funded by the German research initiative "Role of the Middle Atmosphere in Climate" (ROMIC/01LG1206A) funded by the German Federal Ministry of Education and Research in the project "Investigation of the Life Cycle of Gravity Waves" (GW-LCYCLE), and by the Deutsche Forschungsgemeinschaft (DFG) via the Project MSGWaves (GW-TP/DO 1020/9-1 and PACOG/RA 1400/6-1).

References

Alexander, M. J. and Grimsdell, A. W.: Seasonal cycle of orographic gravity wave occurrence above small islands in the Southern Hemisphere: Implications for effects on the general circulation, Journal of Geophysical Research Atmospheres, 118, 11,589–11,599, https://doi.org/10.1002/2013JD020526, 2013.

Alexander, M. J. and Pfister, L.: Gravity wave momentum flux in the lower stratosphere over convection, Geophysical Research Letters, 22, 2029–2032, https://doi.org/10.1029/95GL01984, 1995.

Alexander, M. J., Gille, J., Cavanaugh, C., Coffey, M., Craig, C., Eden, T., Francis, G., Halvorson, C., Hannigan, J., Khosravi, R., Kinnison, D., Lee, H., Massie, S., Nardi, B., Barnett, J., Hepplewhite, C., Lambert, A., and Dean, V.: Global estimates of gravity wave momentum flux from High Resolution Dynamics Limb Sounder observations, Journal of Geophysical Research, 113, D15S18, https://doi.org/10.1029/2007jd008807, 2008.

Balluch, M. G. and Haynes, P. H.: Quantification of lower stratospheric mixing processes using aircraft data, Journal of Geophysical Research Atmospheres, 102, 23 487–23 504, https://doi.org/10.1029/97jd00607, 1997.

Bramberger, M., Dörnbrack, A., Bossert, K., Ehard, B., Fritts, D. C., Kaifler, B., Mallaun, C., Orr, A., Pautet, P. D., Rapp, M., Taylor, M. J., Vosper, S., Williams, B. P., and Witschas, B.: Does Strong Tropospheric Forcing Cause Large-Amplitude Mesospheric Gravity Waves? A DEEPWAVE Case Study, Journal of Geophysical Research: Atmospheres, 122, 11,422–11,443, https://doi.org/10.1002/2017JD027371, 2017.

Bramberger, M., Dörnbrack, A., Wilms, H., Gemsa, S., Raynor, K., and Sharman, R.: Vertically Propagating Mountain Waves—A Hazard for High-Flying Aircraft?, Journal of Applied Meteorology and Climatology, 57, 1957–1975, https://doi.org/10.1175/JAMC-D-17-0340.1, 2018.

Ern, M., Trinh, Q. T., Preusse, P., Gille, J. C., Mlynczak, M. G., Iii, J. M., and Riese, M.: GRACILE: A comprehensive climatology of atmospheric gravity wave parameters based on satellite limb soundings, Earth System Science Data, 10, 857–892, https://doi.org/10.5194/essd-10-857-2018, 2018.

Fritts, D. C. and Alexander, M. J.: Gravity wave dynamics and effects in the middle atmosphere, Reviews of Geophysics, 41, https://doi.org/10.1029/2001RG000106, 2003.

Fritts, D. C., Smith, R. B., Taylor, M. J., Doyle, J. D., Eckermann, S. D., Dörnbrack, A., Rapp, M., Williams, B. P., Pautet, P. D., Bossert, K., Criddle, N. R., Reynolds, C. A., Reinecke, P. A., Uddstrom, M., Revell, M. J., Turner, R., Kaifler, B., Wagner, J. S., Mixa, T., Kruse, C. G., Nugent, A. D., Watson, C. D., Gisinger, S., Smith, S. M., Lieberman, R. S., Laughman, B., Moore, J. J., Brown, W. O., Haggerty, J. A., Rockwell, A., Stossmeister, G. J., Williams, S. F., Hernandez, G., Murphy, D. J., Klekociuk, A. R., Reid, I. M., and Ma, J.: The deep propagating gravity wave experiment (deepwave): An airborne and ground-based exploration of gravity wave propagation and effects from their sources throughout the lower and middle atmosphere, Bulletin of the American Meteorological Society, 97, 425–453, https://doi.org/10.1175/BAMS-D-14-00269.1, 2016.

Geller, M. A., Alexander, M. J., Love, P. T., Bacmeister, J. T., Ern, M., Hertzog, A., Manzini, E., Preusse, P., Sato, K., Scaife, A. A., and Zhou, T.: A comparison between gravity wave momentum fluxes in observations and climate models, Journal of Climate, 26, 6383–6405, https://doi.org/10.1175/JCLI-D-12-00545.1, 2013.

Gettelman, a., Pan, L. L., Randel, W. J., Hoor, P., Birner, T., and Hegglin, M. I.: The Extratropical Upper Troposphere and Lower Stratosphere, Reviews of Geophysics, 49, 1–31, https://doi.org/10.1029/2011RG000355.1.INTRODUCTION, 2011.

Gisinger, S., Dörnbrack, A., Matthias, V., Doyle, J. D., Eckermann, S. D., Ehard, B., Hoffmann, L., Kaifler, B., Kruse, C. G., and Rapp, M.: Atmospheric conditions during the deep propagating gravity wave experiment (DEEPWAVE), Monthly Weather Review, 145, 4249–4275, https://doi.org/10.1175/MWR-D-16-0435.1, 2017.

Grinsted, A., Moore, J. C., and Jevrejeva, S.: Application of the cross wavelet transform and wavelet coherence to geophysical time series, Nonlinear Processes in Geophysics, 11, 561–566, https://doi.org/10.5194/npg-11-561-2004, 2004.

Grubišić, V., Doyle, J. D., Kuettner, J., Mobbs, S., Smith, R. B., Whiteman, C. D., Dirks, R., Czyzyk, S., Cohn, S. A., Vosper, S., Weissmann, M., Haimov, S., De Wekker, S. F. J., Pan, L. L., and Chow, F. K.: THE TERRAIN-INDUCED ROTOR EXPERIMENT, Bulletin of the American Meteorological Society, 89, 1513–1534, https://doi.org/10.1175/2008BAMS2487.1, 2008.

Hegglin, M. I. and Shepherd, T. G.: O3-N2O correlations from the Atmospheric Chemistry Experiment: Revisiting a diagnostic of transport and chemistry in the stratosphere, Journal of Geophysical Research Atmospheres, 112, 1–15, https://doi.org/10.1029/2006JD008281, 2007.

Heller, R., Voigt, C., Beaton, S., Dörnbrack, A., Giez, A., Kaufmann, S., Mallaun, C., Schlager, H., Wagner, J., Young, K., and Rapp, M.: Mountain waves modulate the water vapor distribution in the UTLS, Atmospheric Chemistry and Physics, 17, 14 853–14 869, https://doi.org/10.5194/acp-17-14853-2017, 2017.

Homeyer, C. R., McAuliffe, J. D., and Bedka, K. M.: On the Development of Above-Anvil Cirrus Plumes in Extratropical Convection, Journal of the Atmospheric Sciences, 74, 1617–1633, https://doi.org/10.1175/JAS-D-16-0269.1, 2017.

Hoor, P., Fischer, H., Lange, L., Lelieveld, J., and Brunner, D.: Seasonal variations of a mixing layer in the lowermost stratosphere as identified by the CO-O 3 correlation from in situ measurements, Journal of Geophysical Research: Atmospheres, 107, https://doi.org/10.1029/2000JD000289, 2002.

Jevrejeva, S., Moore, J. C., and Grinsted, A.: Influence of the Arctic Oscillation and El Niño-Southern Oscillation (ENSO) on ice conditions in the Baltic Sea: The wavelet approach, Journal of Geophysical Research: Atmospheres, 108, https://doi.org/10.1029/2003jd003417, 2003.

Kaluza, T., Kunkel, D., and Hoor, P.: On the occurrence of strong vertical wind shear in the tropopause region: a 10-year ERA5 northern hemispheric study, Weather and Climate Dynamics, 2, 631–651, https://doi.org/10.5194/wcd-2-631-2021, 2021.

Kaluza, T., Kunkel, D., and Hoor, P.: Analysis of Turbulence Reports and ERA5 Turbulence Diagnostics in a Tropopause-Based Vertical Framework, Geophysical Research Letters, 49, https://doi.org/10.1029/2022GL100036, https://onlinelibrary.wiley.com/doi/10.1029/2022GL100036, 2022.

Kim, Y., Eckermann, S. D., and Chun, H.: An overview of the past, present and future of gravity-wave drag parametrization for numerical climate and weather prediction models, Atmosphere-Ocean, 41, 65–98, https://doi.org/10.3137/ao.410105, 2003.

Krautstrunk, M. and Giez, A.: The Transition From FALCON to HALO Era Airborne Atmospheric Research, in: Atmospheric Physics: Background - Methods - Trends, edited by Schuman, U., pp. 609–624, Springer-Verlag Berlin Heidelberg, https://doi.org/10.1007/978-3-642-30183-4_37, 2012.

Krisch, I., Preusse, P., Ungermann, J., Dörnbrack, A., Eckermann, S. D., Ern, M., Friedl-Vallon, F., Kaufmann, M., Oelhaf, H., Rapp, M., Strube, C., and Riese, M.: First tomographic observations of gravity waves by the infrared limb imager GLORIA, Atmospheric Chemistry and Physics, 17, 14 937–14 953, https://doi.org/10.5194/acp-17-14937-2017, 2017.

Kunkel, D., Hoor, P., and Wirth, V.: Can inertia-gravity waves persistently alter the tropopause inversion layer?, Geophysical Research Letters, 41, 7822–7829, https://doi.org/10.1002/2014GL061970, 2014.

Lane, T. P. and Sharman, R. D.: Gravity wave breaking, secondary wave generation, and mixing above deep convection in a three-dimensional cloud model, Geophysical Research Letters, 33, 1–5, https://doi.org/10.1029/2006GL027988, 2006.

Lilly, D. K., Waco, D. E., and Adelfang, S. I.: Stratospheric mixing estimated from high-altitude turbulence measurements, Journal of Applied Meteorology and Climatology, 13, 488–493, 1974.

Liu, Y., Liang, X. S., and Weisberg, R. H.: Rectification of the bias in the wavelet power spectrum, Journal of Atmospheric and Oceanic Technology, 24, 2093–2102, https://doi.org/10.1175/2007JTECHO511.1, 2007.

Mahalov, A., Moustaoui, M., and Grubišić, V.: A numerical study of mountain waves in the upper troposphere and lower stratosphere, Atmospheric Chemistry and Physics, 11, 5123–5139, https://doi.org/10.5194/acp-11-5123-2011, 2011.

Mallaun, C., Giez, A., and Baumann, R.: Calibration of 3-D wind measurements on a single-engine research aircraft, Atmospheric Measurement Techniques, 8, 3177–3196, https://doi.org/10.5194/amt-8-3177-2015, 2015.

Mauder, M., Desjardins, R. L., and MacPherson, I.: Scale analysis of airborne flux measurements over heterogeneous terrain in a boreal ecosystem, Journal of Geophysical Research Atmospheres, 112, https://doi.org/10.1029/2006JD008133, 2007.

Moustaoui, M., Mahalov, A., Teitelbaum, H., and Grubišić, V.: Nonlinear modulation of O3 and CO induced by mountain waves in the upper troposphere and lower stratosphere during terrain-induced rotor experiment, Journal of Geophysical Research Atmospheres, 115, https://doi.org/10.1029/2009JD013789, 2010.

Mullendore, G. L., Durran, D. R., and Holton, J. R.: Cross-tropopause tracer transport in midlatitude convection, Journal of Geophysical Research D: Atmospheres, 110, 1–14, https://doi.org/10.1029/2004JD005059, 2005.

Müller, S., Hoor, P., Berkes, F., Bozem, H., Klingebiel, M., Reutter, P., Smit, H. G., Wendisch, M., Spichtinger, P., and Borrmann, S.: In situ detection of stratosphere-troposphere exchange of cirrus particles in the midlatitudes, Geophysical Research Letters, 42, 949–955, https://doi.org/10.1002/2014GL062556, 2015.

Pan, L. L., Randel, W. J., Gary, B. L., Mahoney, M. J., and Hintsa, E. J.: Definitions and sharpness of the extratropical tropopause: A trace gas perspective, Journal of Geophysical Research D: Atmospheres, 109, 1–11, https://doi.org/10.1029/2004JD004982, 2004.

Panofsky, H. A., Dutton, J. A., Hemmerich, K. H., McCreary, G., and Loving, N. V.: Case studies of the distribution of CAT in the troposphere and stratosphere, Journal of Applied Meteorology and Climatology, 7, 384–389, 1968.

Pavelin, E., Whiteway, J. A., Busen, R., and Hacker, J.: Airborne observations of turbulence, mixing, and gravity waves in the tropopause region, Journal of Geophysical Research: Atmospheres, 107, ACL 8–1–ACL 8–6, https://doi.org/10.1029/2001jd000775, 2002.

Podglajen, A., Hertzog, A., Plougonven, R., and Legras, B.: Lagrangian temperature and vertical velocity fluctuations due to gravity waves in the lower stratosphere, Geophysical Research Letters, 43, 3543–3553, https://doi.org/10.1002/2016GL068148, 2016.

Podglajen, A., Bui, T. P., Dean-Day, J. M., Pfister, L., Jensen, E. J., Alexander, M. J., Hertzog, A., Kärcher, B., Plougonven, R., and Randel, W. J.: Small-Scale Wind Fluctuations in the Tropical Tropopause Layer from Aircraft Measurements: Occurrence, Nature, and Impact on Vertical Mixing, Journal of the Atmospheric Sciences, 74, 3847–3869, https://doi.org/10.1175/JAS-D-17-0010.1, 2017.

Press, W. H., Teukolsky, S. A., Vetterling, W. T., and Flannery, B. P.: Numerical Recipes: The Art of Scientific Computing, vol. 56, Cambridge University Press, https://doi.org/10.2307/4830, 1987.

Rapp, M., Kaifler, B., Dörnbrack, A., Gisinger, S., Mixa, T., Reichert, R., Kaifler, N., Knobloch, S., Eckert, R., Wildmann, N., Giez, A., Krasauskas, L., Preusse, P., Geldenhuys, M., Riese, M., Woiwode, W., Friedl-Vallon, F., Sinnhuber, B. M., De la Torre, A., Alexander, P., Hormaechea, J. L., Janches, D., Garhammer, M., Chau, J. L., Federico Conte, J., Hoor, P., and Engel, A.: Southtrac-gw: An airborne field campaign to explore gravity wave dynamics at the world's strongest hotspot, Bulletin of the American Meteorological Society, 102, E871–E893, https://doi.org/10.1175/BAMS-D-20-0034.1, 2021.

Riese, M., Ploeger, F., Rap, A., Vogel, B., Konopka, P., Dameris, M., and Forster, P.: Impact of uncertainties in atmospheric mixing on simulated UTLS composition and related radiative effects, Journal of Geophysical Research Atmospheres, 117, https://doi.org/10.1029/2012JD017751, 2012.

Schilling, T., Lübken, F. J., Wienhold, F. G., Hoor, P., and Fischer, H.: TDLAS trace gas measurements within mountain waves over Northern Scandinavia during the POLSTAR campaign in early 1997, Geophysical Research Letters, 26, 303–306, https://doi.org/10.1029/1998GL900314, 1999.

Schumann, U.: The horizontal spectrum of vertical velocities near the tropopause from global to gravity wave scales, Journal of the Atmospheric Sciences, 76, 3847–3862, https://doi.org/10.1175/JAS-D-19-0160.1, 2019.

Shapiro, M. A.: Turbulent Mixing within Tropopause Folds as a Mechanism for the Exchange of Chemical Constituents between the Stratosphere and Troposphere, Journal of the Atmospheric Sciences, 37, 994–1004, https://doi.org/10.1175/1520-0469(1980)037<0994:tmwtfa>2.0.co;2, 1980.

Sharman, R., Tebaldi, C., Wiener, G., and Wolff, J.: An Integrated Approach to Mid- and Upper-Level Turbulence Forecasting, Weather and Forecasting, 21, 268–287, https://doi.org/10.1175/WAF924.1, 2006.

Sharman, R. D. and Pearson, J. M.: Prediction of Energy Dissipation Rates for Aviation Turbulence. Part I: Forecasting Nonconvective Turbulence, Journal of Applied Meteorology and Climatology, 56, 317–337, https://doi.org/10.1175/JAMC-D-16-0205.1, 2017.

Smith, R. B., Woods, B. K., Jensen, J., Cooper, W. A., Doyle, J. D., Jiang, Q., and Grubişiĉ, V.: Mountain waves entering the stratosphere, Journal of the Atmospheric Sciences, 65, 2543–2562, https://doi.org/10.1175/2007JAS2598.1, 2008.

Smith, R. B., Nugent, A. D., Kruse, C. G., Fritts, D. C., Doyle, J. D., Eckermann, S. D., Taylor, M. J., Dörnbrack, A., Uddstrom, M., Cooper, W., Romashkin, P., Jensen, J., and Beaton, S.: Stratospheric gravity wave fluxes and scales during DEEPWAVE, Journal of the Atmospheric Sciences, 73, 2851–2869, https://doi.org/10.1175/JAS-D-15-0324.1, 2016.

Söder, J., Zülicke, C., Gerding, M., and Lübken, F. J.: High-Resolution Observations of Turbulence Distributions Across Tropopause Folds, Journal of Geophysical Research: Atmospheres, 126, 1–20, https://doi.org/10.1029/2020JD033857, 2021.

Torrence, C. and Compo, G. P.: A Practical Guide to Wavelet Analysis, Bulletin of the American Meteorological Society, 79, 61–78, https://doi.org/10.1175/1520-0477(1998)079<0061:APGTWA>2.0.CO;2, 1998.

Tozer, B., Sandwell, D. T., Smith, W. H., Olson, C., Beale, J. R., and Wessel, P.: Global Bathymetry and Topography at 15 Arc Sec: SRTM15+, Earth and Space Science, 6, 1847–1864, https://doi.org/10.1029/2019EA000658, 2019.

Wang, P. K.: Moisture plumes above thunderstorm anvils and their contributions to cross-tropopause transport of water vapor in midlatitudes, Journal of Geophysical Research: Atmospheres, 108, 2002JD002 581, https://doi.org/10.1029/2002JD002581, 2003.

Whiteway, J. A., Pavelin, E. G., Busen, R., Hacker, J., and Vosper, S.: Airborne measurements of gravity wave breaking at the tropopause, Geophysical Research Letters, 30, 2–6, https://doi.org/10.1029/2003GL018207, 2003.

Woiwode, W., Dörnbrack, A., Bramberger, M., Friedl-Vallon, F., Haenel, F., Höpfner, M., Johansson, S., Kretschmer, E., Krisch, I., Latzko, T., Oelhaf, H., Orphal, J., Preusse, P., Sinnhuber, B.-M., and Ungermann, J.: Mesoscale fine structure of a tropopause fold over mountains, Atmospheric Chemistry and Physics, 18, 15 643–15 667, https://doi.org/10.5194/acp-18-15643-2018, 2018.

Woods, B. K. and Smith, R. B.: Energy flux and wavelet diagnostics of secondary mountain waves, Journal of the Atmospheric Sciences, 67, 3721–3738, https://doi.org/10.1175/2009JAS3285.1, 2010.

Woods, B. K. and Smith, R. B.: Short-Wave Signatures of Stratospheric Mountain Wave Breaking, Journal of the Atmospheric Sciences, 68, 635–656, https://doi.org/10.1175/2010JAS3634.1, 2011.

Wright, C. J. and Banyard, T. P.: Multidecadal Measurements of UTLS Gravity Waves Derived From Commercial Flight Data, Journal of Geophysical Research: Atmospheres, 125, 1–20, https://doi.org/10.1029/2020JD033445, 2020.

Zahn, A. and Brenninkmeijer, C. A.: New Directions: A Chemical Tropopause Defined, Atmospheric Environment, 37, 439–440, https://doi.org/10.1016/S1352-2310(02)00901-9, 2003.

Zhang, F., Wei, J., Zhang, M., Bowman, K. P., Pan, L. L., Atlas, E., and Wofsy, S. C.: Aircraft measurements of gravity waves in the upper troposphere and lower stratosphere during the START08 field experiment, Atmospheric Chemistry and Physics, 15, 7667–7684, https://doi.org/10.5194/acp-15-7667-2015, 2015.